Proposal
for an experiment at the 50-GeV PS

Measurement of the cross sections of Σp scatterings

F. Hiruma, R. Honda, K. Hosomi, H. Kanda, T. Koike, Y. Matsumoto,
K. Miwa(spokesperson), A. Sasaki, K. Shirotori, K. Sugihara, H. Tamura, M. Ukai,
K. Yagi, T.O. Yamamoto, Y. Yonemoto
Tohoku University, Japan

K. Imai, Y. Kondo
Japan Atomic Energy Agency (JAEA), Japan

M. Ieiri, S. Ishimoto, I. Nakamura, M. Naruki, S. Suzuki, H. Takahashi, T. Takahashi,
M. Tanaka, K. Yoshimura
High Energy Accelerator Research Organization (KEK), Japan

T.N. Takahashi
University of Tokyo, Japan

S. Adachi, M. Moritsu, H. Sugimura
Kyoto University, Japan

K. Tanida
Seoul National University, Korea

J.K. Ahn, B.H. Choi
Pusan National University, Korea

S. Callier, C.d.L. Taille, L. Raux
IN2P3/LAL Orsay, France

Abstract

In order to test theoretical frameworks of the baryon-baryon interactions and to confirm the "Pauli effect between quarks" for the first time, we propose an experiment to measure low-energy hyperon proton scattering cross sections in the following channels with high statistics,

1. $\Sigma^- p$ elastic scattering,
2. $\Sigma^- p \to \Lambda n$ inelastic scattering,
3. $\Sigma^+ p$ elastic scattering.

According to theoretical models based on quark-gluon picture for the short range part of the baryon-baryon interactions, the $\Sigma^+ p$ channel is expected to have an extremely repulsive core due to the Pauli effect between quarks, which leads a $\Sigma^+ p$ cross section twice as large as that predicted by conventional meson exchange models with a phenomenologically treated short range repulsive core. In addition, measurement of the $\Sigma^- p$ channel where the quark Pauli effect is not effective is also necessary to test the present theoretical models based on meson exchange picture with the flavor SU(3) symmetry. Thus this experiment will provide essential data to test the frameworks of the theoretical models of the baryon-baryon interactions and to investigate the nature of the repulsive core which has not been understood yet.

In order to overcome the experimental difficulties in measuring low-energy hyperon proton scattering, we will use a new experimental technique in which a liquid H_2 target is used as hyperon production and hyperon scattering targets with a detector system surrounding the LH_2 target for detection of a scattered proton and a decay product from a hyperon. The hyperon scattering event is kinematically identified. Because imaging detectors used in past experiments are not employed, high intensity π beam can be used, allowing us to take high statistics data of 100 times more than the previous experiments.

The experiment is performed at the K1.8 beam line by utilizing the K1.8 beam line spectrometer and the SKS spectrometer. A high intensity π beam of 2×10^7/spill at 1.32 GeV/c is used to produce as many hyperon beam as possible. With 16×10^6 Σ^- beam and 55×10^6 Σ^+ beam around 500 MeV/c which are tagged by the spectrometers, we will detect $\sim$10,000 $\Sigma^- p$ and $\Sigma^+ p$ scattering events and $\sim$6,000 $\Sigma^- p \to \Lambda n$ inelastic reaction events in 60 days beam time in total.

1 Introduction

The nuclear force is one of the most important phenomena which form all the "matter" in nature. However, our understanding of the nuclear force is quite unsatisfactory yet. In view of the current nuclear physics, understanding low energy interactions between hadrons based on QCD is an important problem to be solved. The nuclear force has been extensively studied experimentally by pp and pn scatterings, and its nature is understood well by meson exchange models in a long range attractive region of more than 1 fm. In the short range region, a strongly repulsive core exists and the miraculous balance between the long-range attraction and the short-range repulsion plays essential roles in the formation of the nucleus. However the nature of the short range region where two nucleons overlap is not understood; it is treated phenomenologically in conventional meson exchange models. In this region, it is expected that dynamics of quarks and gluons, the constituents of the nucleon, play an important role, and introducing a new flavor of quarks, a strangeness quark, will provide a clue to approach this problem. Thus, in order to understand the nuclear force, it is crucially important to investigate the generalized baryon-baryon (B_8B_8) interactions including the hyperon nucleon (YN) and the hyperon hyperon (YY) sectors. The theoretical studies of the B_8B_8 interactions have been developed by two different types of theoretical models, one is the one boson exchange model such as Nijmegen OBEP model based on meson exchange picture, and the other is quark based approaches such as Quark Cluster Model (QCM).

The Nijmegen group developed one boson exchange (OBE) models that extend nuclear force to baryon-baryon interactions based on flavor SU(3) symmetry and the phenomenological core potential[1].

Many efforts have been also devoted to understand the B_8B_8 interactions based on the QCD. A direct derivation of these interactions from QCD involves tremendous difficulties, such as the quark confinement and multi-gluon effects in the low energy phenomena. The Quark Cluster Model (QCM) has been developed as a QCD-inspired model which assumes constituent quarks with the color degree of freedom in a confinement potential and takes into account the effect of one gluon exchange between them. In this model, the short range parts of the baryon-baryon interactions are calculated using the resonating group method, where color magnetic interaction from one gluon exchange and the quark Pauli effect are found to play essential roles and the nature of the NN repulsive core is naturally derived[2]. In addition, Kyoto group proposed baryon-baryon interaction models which use the Quark Cluster Model for the short range part and the meson exchange picture in the long range part[3] as a realistic interaction for calculations of YN scattering cross sections and hypernuclear structure.

Recently, a new method to extract the B_8B_8 potentials in the coordinate space from lattice QCD simulations has been proposed and applied to the NN system, and also to YN systems. Figure 1 shows the six independent B_8B_8 potentials for S-wave in the flavor SU(3) limit calculated by a lattice QCD simulation [5]. The newly appeared interactions are predicted to show an interesting characteristics which are different from the NN interaction especially in the short range region. The (8s) component is completely Pauli forbidden for the most compact $(0S)^6$ configuration, where all constituent quarks occupy the 0S state, and is characterized by the strong repulsion originating from the quark Pauli principle. The (10) state is almost Pauli forbidden, and thus the interaction is also strongly repulsive. On the other hand, the (8a) state turns out to have a very weak interaction. The (1) component in the H-particle channel is attractive because of the color-magnetic interaction. The features

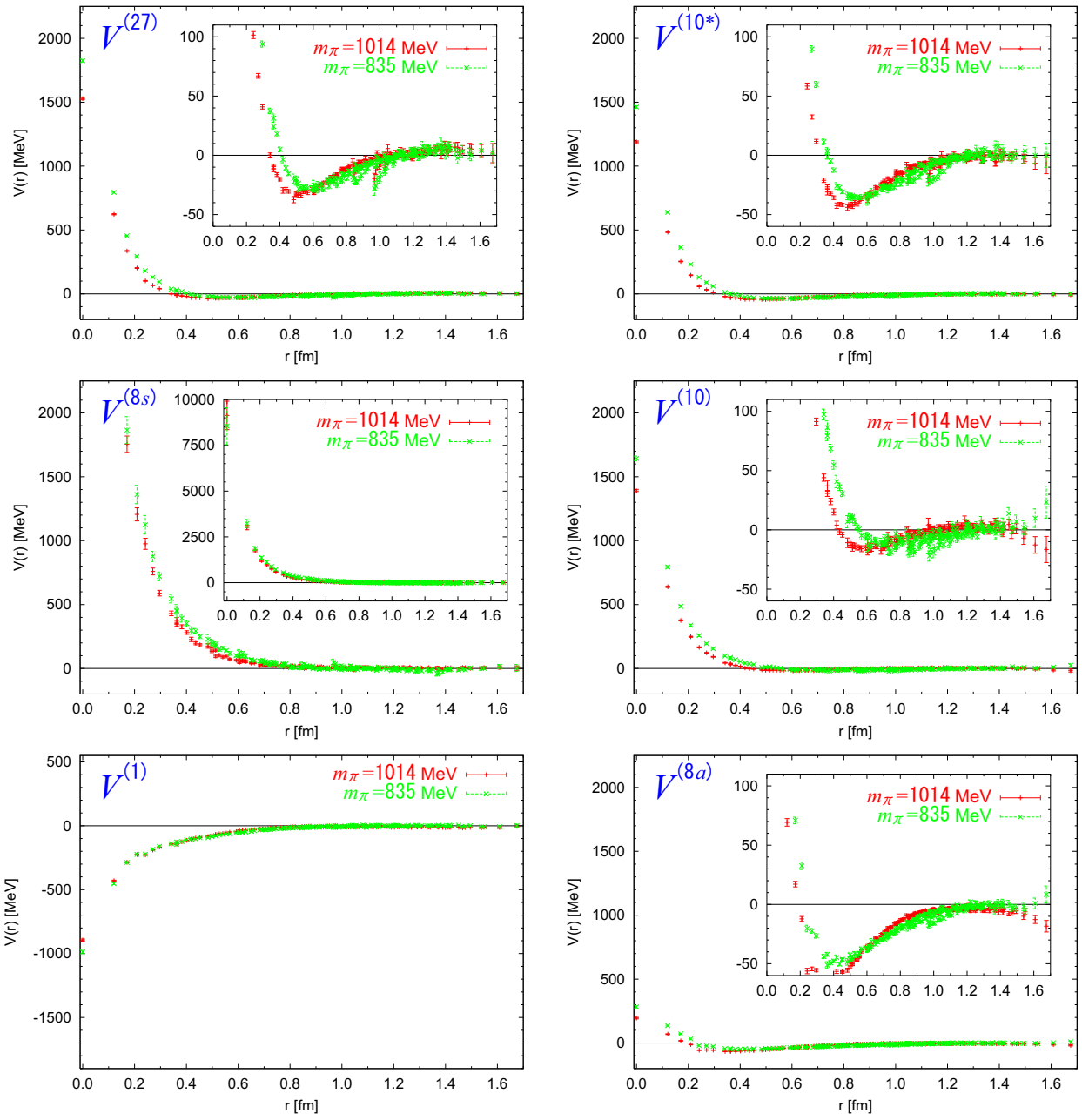

Figure 1: The six independent B_8B_8 potentials for S-wave in the flavor SU(3) limit, extracted from the lattice QCD simulation at m_π =1014 MeV (red bars) and m_π =835 MeV (green bars). [5]

of the calculated potentials completely agree with the Quark Cluster Model prediction. This agreement suggests that the quark Pauli blocking plays an essential role for the repulsive core in B_8B_8 systems as originally proposed in [2].

In order to investigate the B_8B_8 interactions, the hyperon proton scattering experiment is the most powerful method because it enables us to give information on wider flavor channels. Table 1 shows the relationship between the isospin basis and the flavor-SU(3) basis for the B_8B_8 interaction. In order to study the framework of B_8B_8 interactions and to investigate the nature of repulsive core, the ΣN system plays an important role. The ΣN interaction is

S	$B_8B_8(I)$	$P=+1$ (symmetric) ^1E or ^3O	$P=-1$ (antisymmetric) ^3E or ^1O
0	$NN(I=0)$	–	(10^*)
0	$NN(I=1)$	(27)	–
	ΛN	$\frac{1}{\sqrt{10}}[(8s)+3(27)]$	$\frac{1}{\sqrt{2}}[-(8a)+(10^*)]$
-1	$\Sigma N(I=1/2)$	$\frac{1}{\sqrt{10}}[3(8s)-(27)]$	$\frac{1}{\sqrt{2}}[(8a)+(10^*)]$
	$\Sigma N(I=3/2)$	(27)	(10)

Table 1: The relationship between the isospin basis and the flavor-SU(3) basis for the B_8B_8 systems. The heading P denotes the flavor-exchange symmetry, S the strangeness, and I the isospin.

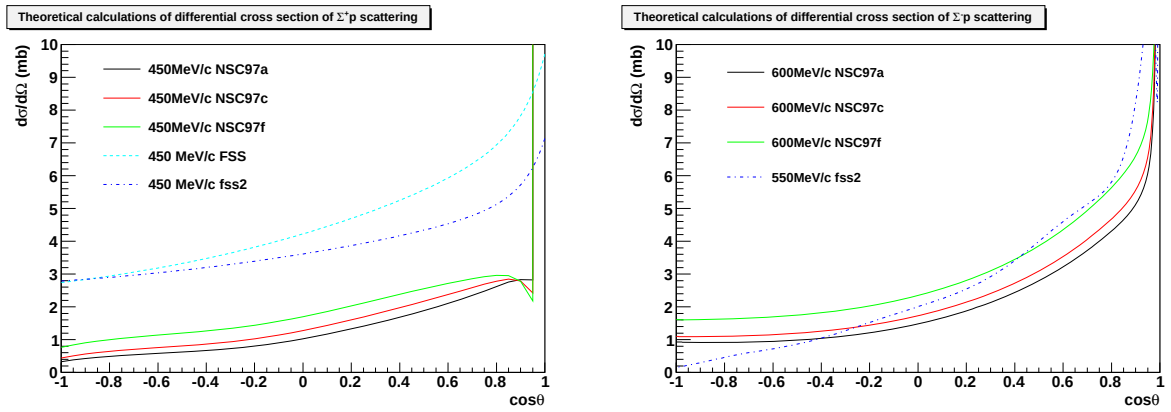

Figure 2: Theoretical predictions by the OBEP (Nijmegen Soft Core) models and the quark cluster (RGM FSS) models for Σ^+p and Σ^-p elastic scatterings. The difference of the differential cross section of Σ^+p channel is originated from a repulsive core due to the quark Pauli effect.

expected to be quite dependent on the configuration of the isospin and spin. Especially, the Σ^+p channel is expected to be very repulsive due to the (10) configuration which is almost Pauli forbidden state. As shown in Table1, the Σ^+p channel is simply described by two multiplets. The spin singlet state is described by the (27) configuration which is the same multiplet as the $NN(I=1)$ interaction. The spin triplet state is represented by the (10) configuration which is expected to be quite repulsive due to the almost Pauli forbidden state. Because the contribution of the triplet state is 3 times larger than the singlet state, the Σ^+p interaction is dominated by the Pauli forbidden state. In the Quark Cluster Model, this strongly repulsive force is derived naturally as the effect of Pauli principle between quarks, while, in the OBE model, such a strongly repulsive force is not obtained. These different strengths of the repulsive forces give sizable differences between the cross sections calculated by these theoretical models as shown in left figure of Figure 2.

On the other hand, in the Σ^-p channel, there is no large difference between cross sections by these two models as shown in right figure of Figure 2, although the Σ^-p channel in $(I=1/2, S(spin)=0)$ includes the (8s) configuration which is completely Pauli forbidden state. It means that the contribution of boson exchange is expected to be large in both theoretical calculations. Therefore measurement of the differential cross section of the Σ^-p

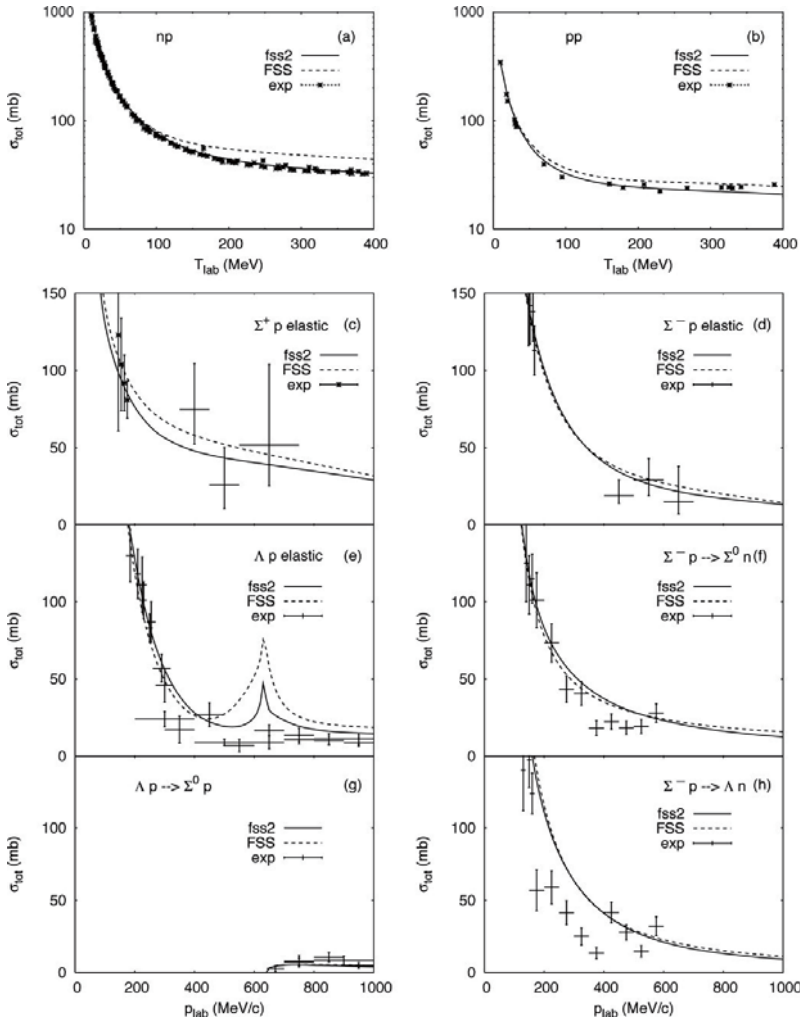

Figure 3: Calculated NN and YN total cross sections by QCM, fss2 (solid curves) and FSS (dashed curves), compared with the experimental data. This data is cited from [4].

($\rightarrow \Lambda n$) channel provides a decisive test for the theoretical models based on meson exchange picture with the flavor SU(3) symmetry. Once the meson exchange theoretical model is confirmed by the $\Sigma^- p$ data, the $\Sigma^+ p$ data allow us to investigate the quark Pauli effect in the short range by comparing the data with theoretical predictions by QCM and OBEP.

Therefore it is essential to measure the scattering data of the $\Sigma^{\pm} p$ and $\Sigma^- p \rightarrow \Lambda n$ reactions to develop the whole picture of the $B_8 B_8$ interaction.

1.1 Historical background of YN scattering experiment and the ΣN interaction

In contrast to the abundant NN scattering data, the YN scattering data are very limited as shown in Figure 3 and in Figure 4 which show the total cross sections and the differential cross sections, respectively. The reason for this poor statistics is the short lifetime of the hyperons. Therefore the experiments require imaging detectors to recognize the complicated reaction topologies in a region of $\sim$cm. In the 1960's, almost all experiments were performed

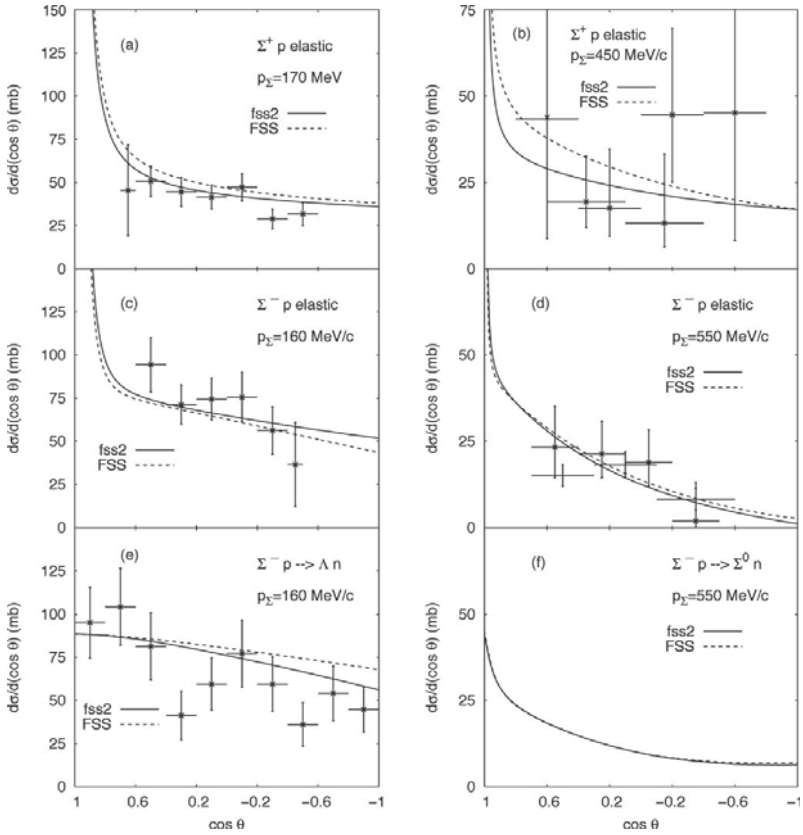

Figure 4: Calculated $\Sigma^+ p$ and $\Sigma^- p$ differential cross sections by fss2 (solid curves) and FSS (dashed curves), compared with the experimental angular distributions. This data is cited from [4].

with bubble chambers. Because the bubble chambers required a low beam rate, a stopping K^- method was often used as the most efficient way to produce hyperons. Therefore the data of the bubble chamber were limited to the low momentum hyperon beam regions (~ 200 MeV/c). The bubble chamber was a suitable detector for a low energy hyperon scattering because it serves as the hyperon production as well as hyperon scattering targets while the low density of liquid hydrogen enables us to see a long track of the scattered proton. However the bubble chamber was an untriggerable detector and could not be operated under a high beam rate. Those are why the statistics is very limited.

Since the YN scattering experiments are difficult, information on the YN interactions have been investigated through hypernuclear data, although extraction of the two-body interaction from nuclear many-body systems suffers from theoretical difficulties. For the ΛN interaction, Λ hypernuclear data via the (K^-, π^-) and (π^+, K^+) reactions provide the Λ-nuclear potential depth and consequently the Λ-nucleon spin-averaged interaction strength, and the high resolution γ-ray spectroscopy of Λ hypernuclei enables us to derive the spin dependent ΛN interactions from the level structure of the Λ hypernuclei [7]. On the other hand, other YN interactions are not yet well understood. For the ΣN interaction, the $\Sigma^\pm p$ scattering experiments were performed at the KEK PS in order to measure the differential cross section in the higher beam momentum region [8, 9, 10]. In these experiments, a scintillation fiber (SCIFI) active target, which is a triggerable imaging detector, was used

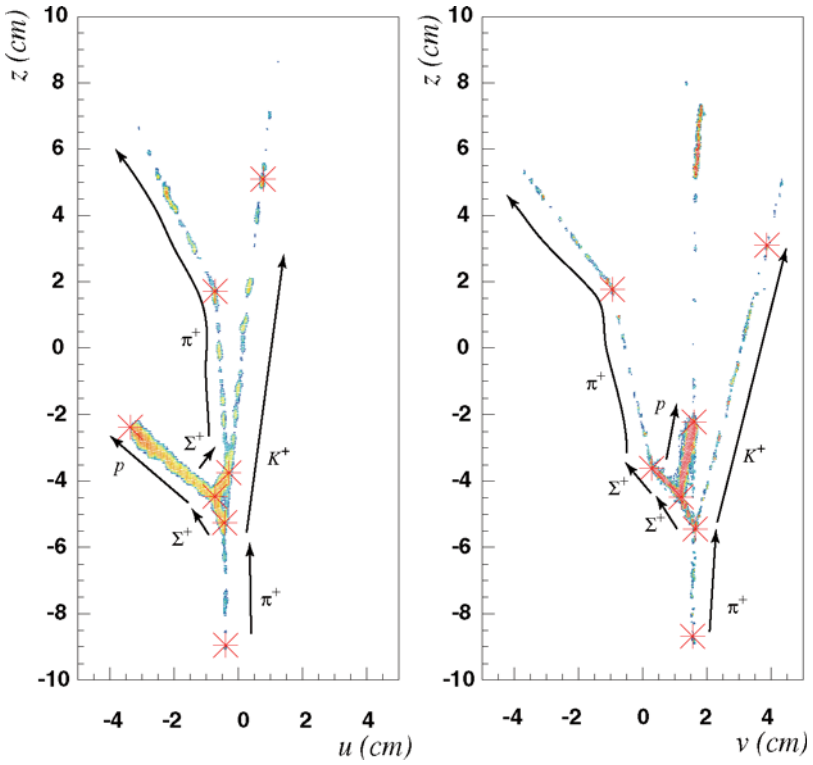

Figure 5: Typical image data, which was identified as $\Sigma^+ p$ elastic scattering for the two different 2 dimensional plane, $u-z$ plane and $v-z$ plane. This figure is cited from [9].

to recognize the scattering events. As shown in Figure 5, the image was efficiently taken triggered by a Σ hyperon production identified by the magnetic spectrometer. The experiment provided the differential cross sections of the $\Sigma^- p$ and $\Sigma^+ p$ elastic scatterings in the higher momentum region of $0.4 < p(\mathrm{GeV}/c) < 0.6$ for the first time. However the statistics was again limited to $\sim$30 events and was insufficient to test the different theoretical models. The main reason was the limited π beam intensity of $\sim 2 \times 10^5$/spill, because the image intensifier tube used to read out the SCIFI target was slow and the images of different events overlapped in the higher beam intensity. The carbon nuclei in the SCIFI target of $(\mathrm{CH})_n$ also caused a background of the quasi-free scattering between a proton inside the carbon nucleus and the Σ beam. Thus, the quality of the scattering data was not improved from the old bubble chamber experiments.

In the case of ΣN interaction, extracting information on the interaction from hypernuclear data is also difficult. The bound state of a Σ hypernuclei was also searched for and only the ${}^{4}_{\Sigma}\mathrm{He}$ $(T = 1/2, S = 0)$ bound state was observed [12]. However, the heavier Σ hypernuclear data exhibited no bound state peaks, suggesting a large conversion width and a shallow or repulsive potential for the spin-isospin averaged Σ nuclear potential. A recent experiment at KEK measured quasi-free Σ production spectra via the (π^-, K^+) reaction on medium and heavy nuclei [13]. The data imply that the spin-isospin averaged Σ nuclear potential is strongly (> 30 MeV) repulsive[14, 15]. However, it is rather difficult to draw a quantitative conclusion on the interaction strength from the Σ-nuclear continuum spectrum.

Therefore, the high statistics scattering data of the Σp channels are highly desired.

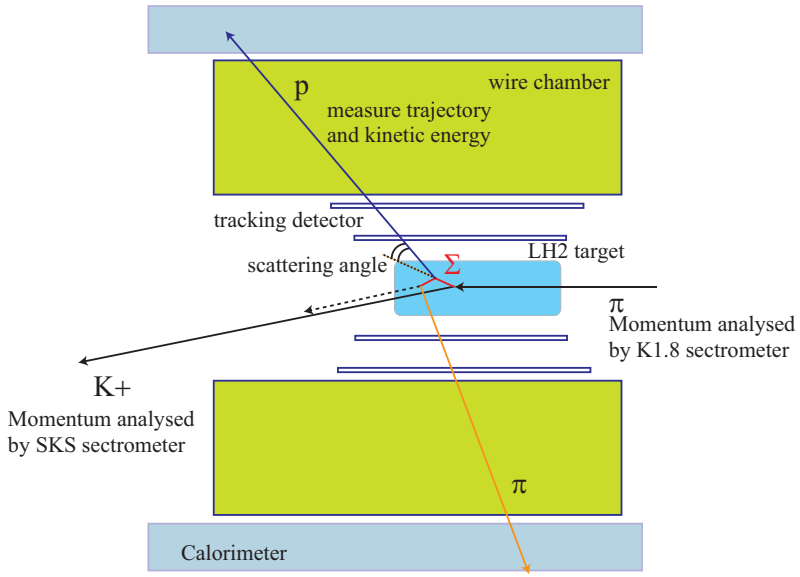

Figure 6: Conceptual experimental setup for the YN scattering using a liquid hydrogen target and the surrounding detectors. The Σ beam is tagged by the detection of the incident π beam and the outgoing K^+ with the beam line spectrometer and the SKS spectrometer, respectively. The surrounding detector is used for the detection of the recoil proton and the decay product of the hypron. The reaction kinematics of the Σp scattering can be reconstructed from the information of the Σ beam and the recoil proton.

1.2 Experimental goal

We propose an experiment to measure the $\Sigma^- p$ and the $\Sigma^+ p$ elastic scattering cross sections and the $\Sigma^- p \to \Lambda n$ reaction cross section with 100 times larger statistics than the previous experiments. From the experience of the past experiments, we designed new experimental setup and conditions by considering the following points:

- High rate meson beam should be handled to produce intense hyperon beam.
- Liquid hydrogen should be used as hyperon production and hyperon-proton scattering targets to be free from the unwanted background such as a quasi-free scattering on other nuclei.
- A sophisticated trigger system should be developed for the efficient selection of the hyperon production and the hyperon scattering events under the high intensity meson beam.

Figure 6 shows the conceptual experimental setup. We use a liquid hydrogen (LH_2) target as hyperon production and hyperon-proton scattering targets. The tracking detectors are placed surrounding the LH_2 target to detect the scattered proton and the decay product from the hyperon. For the scattered proton, its trajectory and the kinetic energy are measured by the detectors surrounding the LH_2 target. Since the momentum vector of the Σ beam can be reconstructed by the beam line and the forward spectrometers, the scattering angle can be obtained by the angle defined by the Σ^- beam and the scattered proton. These three measurements, namely the Σ beam momentum, the scattering angle, and the energy

$\Sigma^- p$ channel	
$\Sigma^- p$ elastic scattering	$\Sigma^- p \to \Sigma^-$"p"
	$\Sigma^- \to \pi^- n$
$\Sigma^- p \to \Lambda n$ inelastic scattering	$\Sigma^- p \to \Lambda n$
	$\Lambda \to \pi^-$"p"
$\Sigma^- p \to \Sigma^0 n$ inelastic scattering	$\Sigma^- p \to \Sigma^0 n$
	$\Sigma^0 \to \Lambda\gamma$, $\Lambda \to \pi^-$"p"
Scattering with Σ^- decay product	
np scattering	$\Sigma^- \to \pi^- n$
	$np \to n$"p"
$\pi^- p$ elastic scattering	$\Sigma^- \to \pi^- n$
	$\pi^- p \to \pi^-$"p"
$\Sigma^+ p$ channel	
$\Sigma^+ p$ elastic scattering	$\Sigma^+ p \to \Sigma^+$"p"
	$\Sigma^+ \to \pi^+ n$ or $\Sigma^+ \to \pi^0$"p"
Σ^+ decay	$\Sigma^+ \to \pi^0$"p"
Scattering with Σ^+ decay product	
pp scattering	$\Sigma^+ \to \pi^0 p$
	$pp \to$"p""p"
np scattering	$\Sigma^+ \to \pi^- n$
	$np \to n$"p"
$\pi^+ p$ elastic scattering	$\Sigma^+ \to \pi^+ n$
	$\pi^+ p \to \pi^+$"p"

Table 2: Summary of the background of the Σp scattering. The main background is the proton scattered by the decay products of Σ. In the $\Sigma^+ p$ scattering, the proton from the Σ^+ also causes a large background.

of the scattered proton, combined with the use of the LH_2 target enable us to identify the scattering event. This is because the reaction is two body reaction and thus its kinematics is uniquely determined.

Since the detectors to identify the scattering event are not be irradiated to the beam, high intensity beam can be used. On the other hand, the difficulty of this technique is to distinguish the scattered proton from other protons such as those from the hyperon decay. Other background source is the proton scattered by the hyperon decay products. Table 2 summarizes the background reactions. The strategy of the experiment is as follow. Since the decay channel of Σ^- is only $n\pi^-$ and there is no decay channel to proton, we will first perform a $\Sigma^- p$ scattering experiment and establish the experimental method. Then we apply this method to a $\Sigma^+ p$ scattering experiment where there are much larger background due to the $\Sigma^+ \to p\pi^0$ decay. In order to remove such background, at least two particles, the scattered proton and the π^+ or proton from the Σ^+ decay, should be detected.

The expected results studied by the simulation are shown in Figure 7, 8 and 9 for the $\Sigma^+ p$, $\Sigma^- p$ and $\Sigma^- p \to \Lambda n$ reactions, respectively, with the two theoretical calculations, the Nijmegen model and the Quark Cluster Models. The assumed cross section in the simulation is 30 mb with a flat angular distribution. The reproduced distribution in Figure 7, 8 and 9

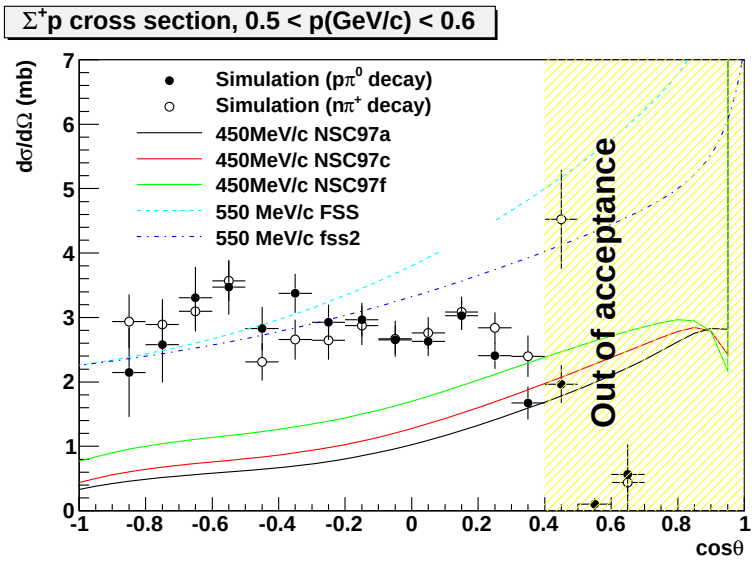

Figure 7: Simulated differential cross section of the $\Sigma^+ p$ scattering in the momentum range of $0.5 < p$ (GeV/c) < 0.6 for the 55×10^6 tagged Σ^+ beam. The black close circle and open circle represent the simulation results for the $p\pi^0$ and $n\pi^+$ modes, respectively. Theoretical predictions by the OBEP (Nijmegen Soft Core) models and the quark cluster (RGM FSS) models are shown.

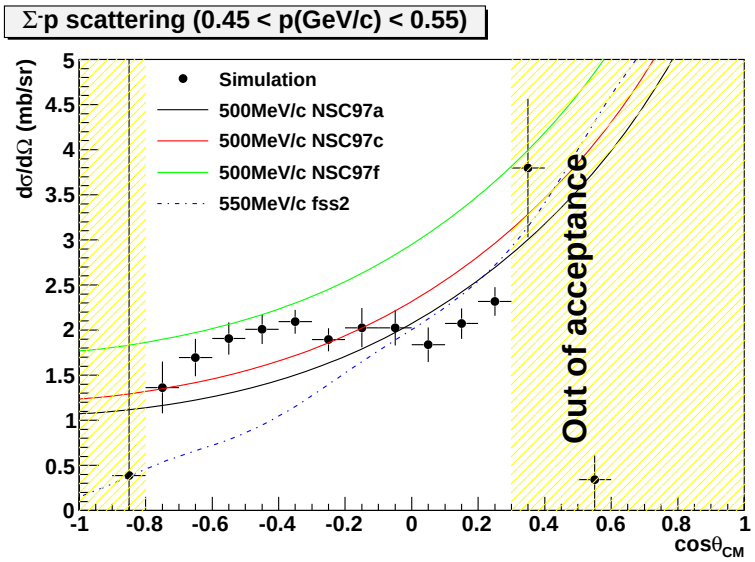

Figure 8: Simulated differential cross section of the $\Sigma^- p$ scattering in the momentum range of $0.45 < p$ (GeV/c) < 0.55 for the 16×10^6 tagged Σ^- beam. The black close circle represents the simulation results. Theoretical predictions by the OBEP (Nijmegen Soft Core) models and the Quark Cluster Models (RGM FSS) are shown.

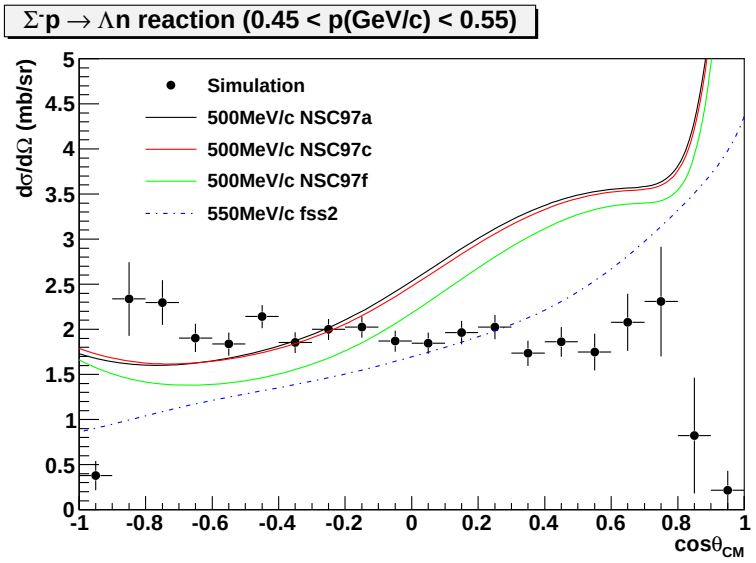

Figure 9: Simulated differential cross section of the $\Sigma^- p \to \Lambda n$ inelastic scattering in the beam momentum regions of $0.45 < p$ (GeV/c) < 0.55 with the theoretical predictions by the OBEP (Nijmegen Soft Core) models and by the Quark Cluster Models (RGM FSS).

shows a flat distribution with fluctuations. This shows the feasibility of the new experimental technique.

For the $\Sigma^+ p$ scattering, the Quark Cluster Model predicts a larger cross section than the OBEP model due to different treatment of the repulsive core as shown in Figure 7. The aim of the $\Sigma^+ p$ channel is to provide a cross section data sufficient to confirm the effect of the strongly repulsive core originating from the quark Pauli effect which appears as the difference of the differential cross section. According to our simulation, the differential cross sections, which were derived separately for the different decay modes of Σ^+, were obtained from ∼2,000 and ∼3,000 scattering events in the momentum region of $0.5 < p$ (GeV/c) < 0.6 for the $p\pi^0$ and $n\pi^+$ modes, respectively. The expected result is sufficient to test the theoretical models and to give information about the nature of the repulsive core.

The two theoretical calculations show similar behavior in the $\Sigma^- p$ elastic scattering and the $\Sigma^- p \to \Lambda n$ inelastic scattering as shown in Figure 8 and 9. In these channels, we aim to measure the angular dependence of the differential cross section with enough statistics and accuracy to test the framework of theoretical models based on meson exchange picture with the flavor SU(3) symmetry, since there is no quark Pauli effect in this channel and the other part of the interaction is essentially the same. The simulated spectra shown in Figure 8 and 9 were obtained from ∼5,000 and ∼4,000 scattering events, respectively, in the momentum region of $0.45 < p$ (GeV/c)< 0.55. This data quality enables us to compare the angular dependence of the differential cross section with the theoretical models and check the theoretical framework for the first time. If theoretical models can reproduce the $\Sigma^- p$ data and there is a difference in the $\Sigma^+ p$ channel, the difference is ascribed to the quark contribution in the $B_8 B_8$ interaction.

As an important feature of scattering experiments, the energy dependence of the cross section is related to the shape of the potential. Especially, in order to investigate the short range repulsive core, the differential cross section of the S-wave has an essential informa-

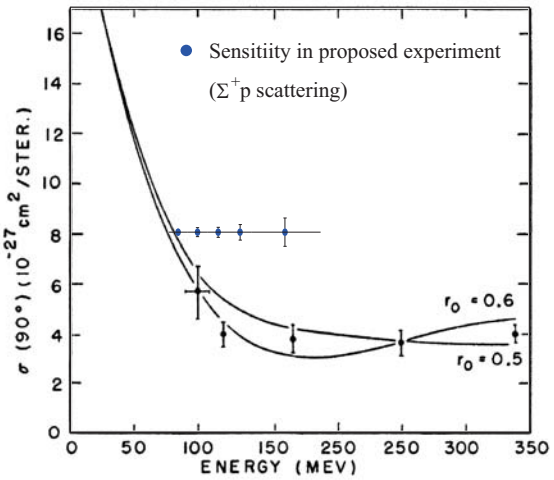

Figure 10: First estimate of the hard core radius of the nuclear force by R. Jastrow [16]. The differential cross section of the pp scattering at 90° is shown with theoretical predictions with different core radius assumptions. The blue points show the sensitivity for the Σ^+p scattering, where the absolute value has no meaning.

tion. In the partial wave analysis, the differential cross section is described by the following equation,

$$\frac{d\sigma}{d\Omega} = \frac{1}{k^2}\Big|\sum_{l=0}^{\infty}(2l+1)e^{i\delta_l}\sin\delta_l P_l(\cos\theta)\Big|^2. \quad (1)$$

Because $P_l(0)$ is 0 for odd l, the S-wave contribution is large for the differential cross section at $\theta = 90^o$. For the NN interaction, the repulsive core radius was estimated from the energy dependence of the differential cross section at $\theta = 90^o$ by R. Jastrow before the precise partial wave analysis as shown in Figure 10. The differential cross section data were compared with calculations in which the repulsive core was represented by a hard sphere, with the radii of 0.5 and 0.6×10^{-13} cm [16]. At present the YN interactions are in a similar situation to Figure 10 and the precise partial wave analysis is still difficult in the proposed experiment. However, the energy dependence provides quite important information and the value at $\theta = 90^o$ is directory connected to the phase shift δ_0. In Figure 10, the sensitivity for the energy dependence of the Σ^+p differential cross section around 90 degree ($-0.1 < \cos(\theta) < 0.1$) in the proposed experiment is overwritten with the pp data. Although the energy is still limited around $80 < E_{kin}$ (MeV) < 170, this will be the first data of energy dependence with enough sensitivity. For the low energy region, the bubble chamber data can be referred. The higher energy region will be obtained by changing the detection angle of the K^+ where we need the different experimental setup. By accumulating the energy dependent data, we can experimentally provide the information about the repulsive core. The proposed experiment is the 1st step toward this goal.

In this proposal, we present not only the experimental method but also the detailed analysis of the simulation data to verify the feasibility of the proposed experiment.

2 Yield estimation and beam time request

Before describing details of the experiment and the analysis method, we present the beam time request and the experimental conditions. Based on this beam time, we performed simulation studies described in the later sections.

The requested beam time is summarized in Table 3. The beam time is estimated based on the experimental conditions summarized in Table 4. We request 16×10^6 tagged Σ^- beam and 55×10^6 tagged Σ^+ beam to detect $\sim$10,000 scattering events for each beam. It takes $\sim$ 20-day beam time for each beam to accumulate the number of Σ beams, assuming that 2×10^7/spill π beam is used. Here the spill is the 2 sec. of flat-top in the 6 sec. time period. In addition to the data taking, we request a tuning time of 5 days which includes the beam tuning, operation check of the K1.8 and SKS systems, and commissioning of the newly installed detector systems. We also study the trigger rate by SKS with and without the fiber system. As a calibration data, pp scattering or πp scattering is also taken to measure the systematics of our experimental method.

At first, we will perform the $\Sigma^- p$ scattering experiment, because in this reaction the background level is much smaller and this channel is suitable to check the feasibility of the present experimental method. After we analyze the data of the $\Sigma^- p$ channel and prove the experimental feasibility. After this check, the $\Sigma^+ p$ scattering should be carried out.

$\Sigma^- p$ scattering experiment	
Detector tuning and trigger study	5 days
Data taking of $\Sigma^- p$ scattering	24 days
Calibration data taking	3 days
$\Sigma^+ p$ scattering experiment	
Detector tuning and trigger study	5 days
Data taking of $\Sigma^- p$ scattering	20 days
Calibration data taking	3 days

Table 3: Beam time request for each scattering experiment.

	$\Sigma^- p$ scattering
Σ^- production cross section	245 μb
π^- beam intensity	2×10^7/spill (2sec beam time in 6 sec cycle)
LH_2 target thickness	30 cm
Acceptance of SKS	4.5%
Survival rate of K^+	34%
DAQ live time	70%
Analysis efficiency	70%
Tagged Σ^-/spill	45/spill
Tagged Σ^-/day	6.6×10^5/day
Accumulated Tagged Σ^-	16×10^6 (24 days)
$\Sigma^- p$ scattering cross section	30 mb (assumption)
$\Sigma^- p$ scattering probability	0.22%
Detection efficiency of scattered proton	35%
$\Sigma^- p$ detection number	11,800

	$\Sigma^+ p$ scattering
Σ^+ production cross section	523 μb
π^+ beam intensity	2×10^7/spill (2sec beam time in 6 sec cycle)
LH_2 target thickness	30 cm
Acceptance of SKS	7.0%
Survival rate of K^+	40%
DAQ live time	70%
Analysis efficiency	70%
Tagged Σ^+/spill	183/spill
Tagged Σ^+/day	2.6×10^6/day
Accumulated Tagged Σ^+	55×10^6 (20 days)
$\Sigma^+ p$ scattering cross section	30 mb (assumption)
$\Sigma^+ p$ scattering probability	0.12%
Detection efficiency of two p's ($\Sigma^+ \to p\pi^0$)	13%
Detection efficiency of p and π^+ ($\Sigma^+ \to n\pi^+$)	21%
$\Sigma^+ p$ detection number ($p\pi^0$ decay mode)	4,400
$\Sigma^+ p$ detection number ($n\pi^+$ decay mode)	7,000

Table 4: Yield estimation of the $\Sigma^- p$ and $\Sigma^+ p$ scatterings.

3 Experimental setup

For this experiment, we plan to utilize the SKS spectrometer and the K1.8 beam line spectrometer at the K1.8 beam line. In addition to the normal K1.8 experimental setup, we newly install a detector system dedicated for the proposed experiment which includes a liquid hydrogen target and the surrounding detectors of fiber tracker, drift chamber and calorimeters in order to detect the scattered proton and the charged particles from hypron decay.

3.1 Magnetic spectrometers to tag Σ beams

In order to identify the $\pi^{\pm}p \to K^{+}\Sigma^{\pm}$ reactions and to measure the Σ hyperon beams, the SKS spectrometer and the K1.8 beam line spectrometer are utilized. Figure 12 shows the experimental setup of the K1.8 beam line and the SKS spectrometers. We use the π^{-} beam of 1.325 GeV/c for the Σ^{-} production and the π^{+} beam of 1.419 GeV/c for the Σ^{+} production, respectively. Figure 11 shows the differential cross section for the $\Sigma^{\pm}$ productions with these reactions [17, 18]. The production cross sections with the π beams are $\sim$5 times smaller than that with K^{-} beam [19]. However, we select π beams for the following reasons. The (K^{-}, π^{-}) reaction suffers from the background of the K^{-} decay. On the other hand, the (π, K^{+}) reaction can identify the Σ production without any background. When the forward scattered K^{+} is detected by the forward spectrometer, the momentum of the Σ hyperons produced by the $\pi p \to K^{+}\Sigma$ reaction is larger than 400 MeV/c. If the scattered π from the $K^{-}p \to \pi\Sigma$ reaction is detected by the forward spectrometer, the momentum of the hyperon is $\sim$ 200 MeV/c and the hypron decays immediately. Therefore, at first, we should establish the experimental method using the π beams.

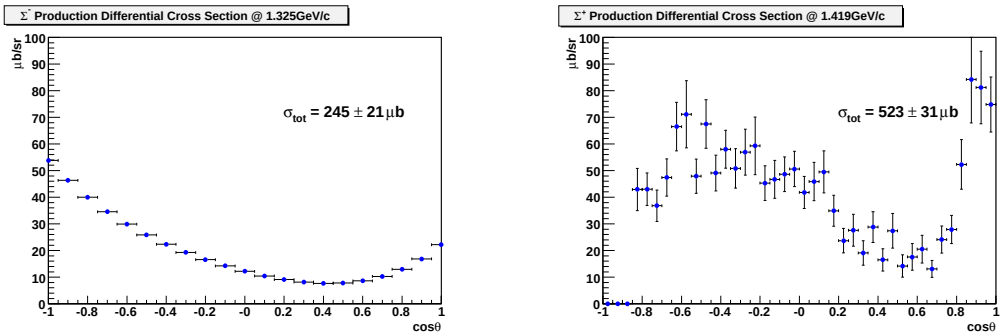

Figure 11: Differential cross sections of the $\pi^{\pm}p \to K^{+}\Sigma^{\pm}$ reactions. The left and right figures show the Σ^{-} production using the 1.325.GeV/c π^{-} beam [17] and the Σ^{+} production using the 1.419.GeV/c π^{+} beam [17], respectively. The θ represents the angle of the scattered K^{+} in the center of mass system.

In order to obtain intense Σ beams, the intensity of the incident π beam is required to be 10^{7} Hz, which corresponds to 2×10^{7}/spill in 2 sec. extraction time during 6 sec. cycle. The spill of the current slow extraction has a spike structure where very intense beam comes instantaneously. The present beam rate is determined by this beam structure. At the K1.8 beam line, two MWPC's (BC1,2) and two MWDC's (BC3,4) are installed upstream and downstream of the beam line spectrometer magnet, respectively. These chambers are

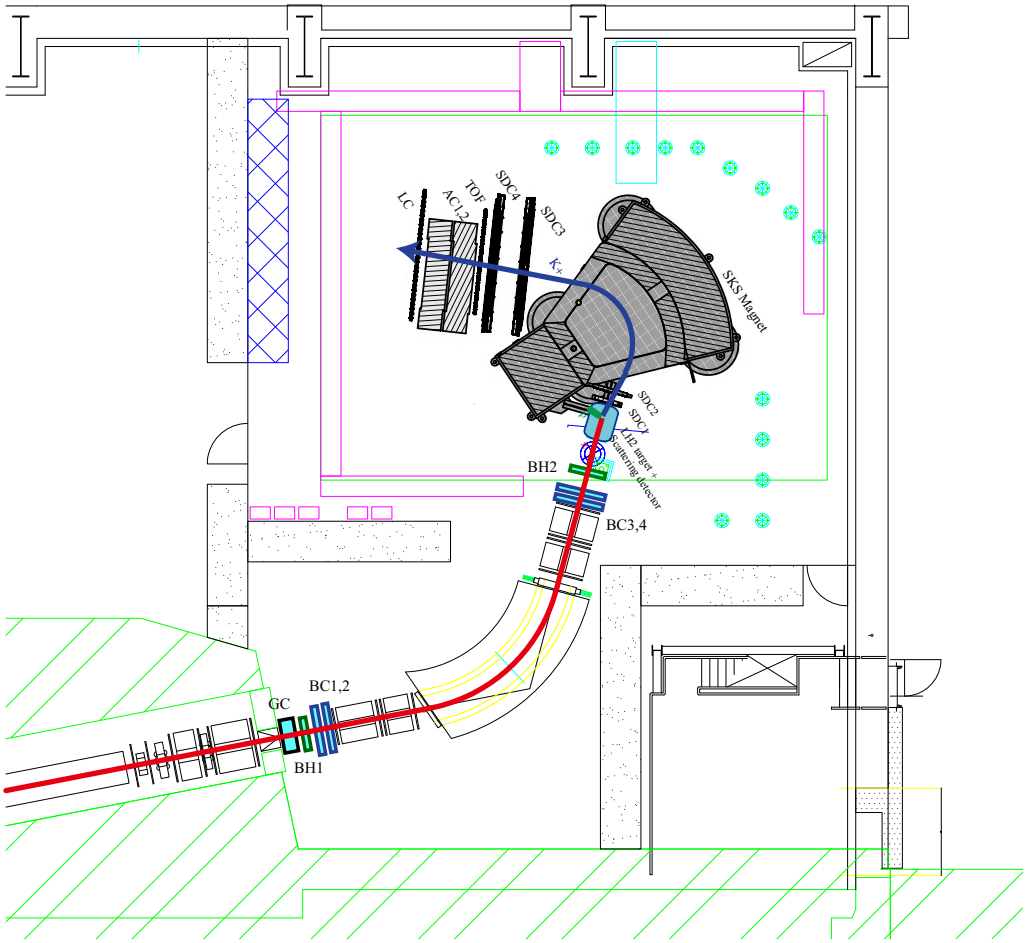

Figure 12: Experimental setup of the K1.8 beam line. The K1.8 spectrometer and the SKS spectrometer analyze the incident π beam particle and the scattered K^+, respectively.

originally designed to work at 10^7 Hz beam rate. However it is difficult to operate these chambers in the present beam condition. In these situation, in order to handle the high intensity π beam, the fiber tracker will be used, which is stable for the high intensity beam and has a better time resolution of 1 nsec. This better time resolution enables us to separate the real beam particle, which interacts at the target, from the accidental beam. The incident π beam particles are defined by the two beam hodoscopes (BH1,2) placed about 11 m apart. The electron contamination is rejected by a gas cherenkov counter placed upstream of BH1. The momenta of the incident π beam particles are analyzed by the K1.8 beam line spectrometer which consists of QQDQQ magnet system and beam line fiber trackers. The original momentum resolution of the K1.8 beam line spectrometer is 0.014 % in rms. The usage of the fiber trackers makes the resolution worse due to the multiple scattering. However, the resolution is acceptable for the proposed experiment. The readout system of the fiber tracker will be the same technology with the fiber vertex tracker which is described in the next subsection. The PPD (MPPC) and the special readout board using an ASIC (SPIROC-A) [20] for PPD are used.

Scattered K^+'s are detected with the SKS spectrometer. The magnetic field is set to 2.1 T for the $\pi^- p \to K^+\Sigma^-$ reaction with 1.3 GeV/c π^- beam. For the Σ^+ production

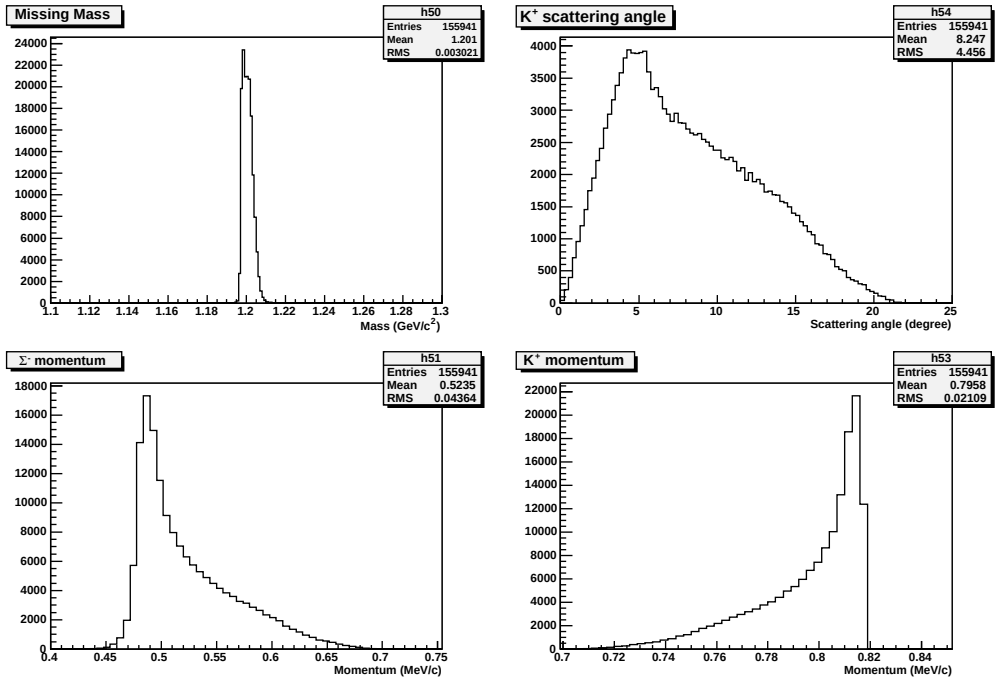

Figure 13: Left-Top: Expected missing mass spectrum of Σ^-. Right-Top: Angular distribution of the scattered K^+. Left-Down: Σ^- momentum distribution. Right-Down: K^+ momentum distribution.

via the $\pi^+ p \rightarrow K^+\Sigma^+$ reaction, we use 1.4 GeV/c π^+ beam, where the magnetic field is increased up to 2.4 T. The momentum of each outgoing particle is analyzed with four drift chambers (SDC1,2,3,4) located upstream and downstream of the SKS magnet. For particle identification, trigger counters (TOF, AC1·2, LC) are placed downstream of SDC4. For the identification of K^+, hits of TOF and LC and veto of AC are required.

The function of the spectrometers is to tag as many Σ beams as possible with good momentum and angular resolutions. The usage of the high intensity beam will cause multi-track events for the beam and scattered particles. However the combination of these multi tracks can be solved so as to have the Σ particle mass. Figure 13 shows the expected missing mass of Σ^- and the kinematical values for the $\pi p \rightarrow K^+\Sigma$ reactions. The acceptances of the SKS for the Σ^- and Σ^+ reactions are 4.5% and 7.0%, respectively, taking into account the target positon in the present experiment. Here the angular distributions of the K^+ of Figure 11 is taken into account. The momenta of the scattered K^+ are $\sim$0.8 GeV/c and $\sim$0.97 GeV/c for the Σ^- and Σ^+ productions, respectively. Because the distance between the target and LC wall is $\sim$7.2 m, the survival rates of the K^+'s are 34 % and 41 %, respectively.

The Σ^- beam momentum has a peak at 0.49 GeV/c and ranges from 0.45 to 0.7 GeV/c as shown in Figure 13. For the Σ^+, beam momentum has a peak at 0.45 GeV/c and ranges from 0.42 to 0.65 GeV/c.

3.1.1 Performance of the spectrometer

The Σ^- beam is identified from the missing mass of the $\pi^- p \rightarrow K^+ X$ reaction. In this simulation, we assumed that the position resolutions of chambers are 200 μm. The left-up

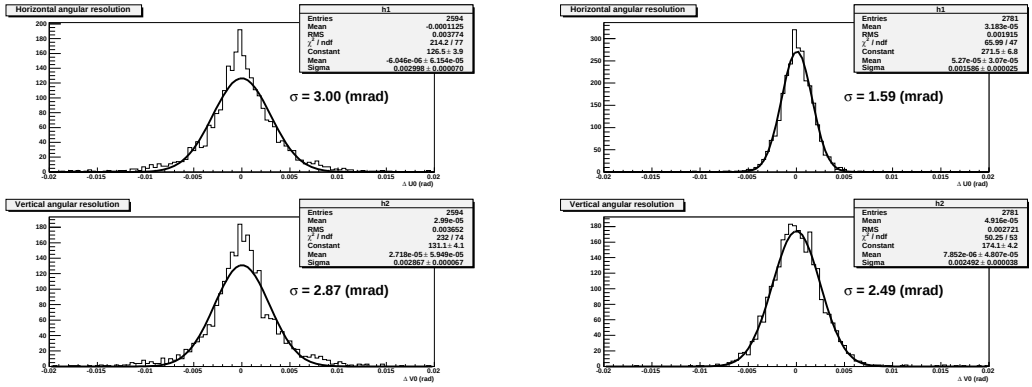

Figure 14: Angular resolution of the SKS (left) and beam line spectrometer (right) at the target. The top figures and down figures show the horizontal and vertical scattering angler resolution, respectively.

panel in Figure 13 shows the missing mass spectrum of the $\pi^- p \to K^+ X$ reaction which shows the clear peak of Σ^-. Because there is no background reaction, the Σ^- can be clearly identified. The width of the peak is estimated to be 3.5 MeV (FWHM).

The momentum of the Σ^- beam should be calculated from the momenta of π^- beam and scattered K^+ and the scattering angle between them. The momentum resolution of the K^+ is expected to be 3 MeV/c which corresponds to $\Delta p/p = 3.8 \times 10^{-3}$. The momentum resolution of π^- is expected to be one order better. Figure 14 shows the angular resolution of the SKS and the beam line spectrometers at the vertex position. From the simulation, the scattering angle of the K^+ is reconstructed with the resolution of 0.18 degree.

Momentum of a Σ^- beam is reconstructed from the momenta of π^- beam and K^+ and the scattering angle. Figure 15 shows the momentum and angular resolutions of the reconstructed Σ^- beam which are obtained to be $\sigma = 6.13$ MeV/c and $\sigma = 0.37$ degree, respectively.

3.1.2 The (π, K) trigger rate

The (π, K) trigger is defined as

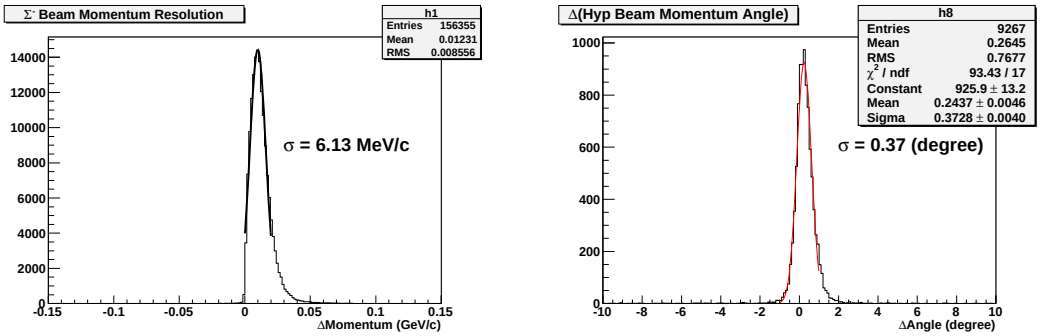

Figure 15: Momentum resolution and angular resolution of a hyperon beam.

Reaction	Beam intensity	(π, K) trigger rate	
Σ^- production	10^6/spill	145/spill	
Σ^+ production	4.3×10^5/spill	120/spill	
	For the present experiment		
Reaction	Beam intensity	(π, K) trigger rate	Real Σ production rate
Σ^- production	2×10^7/spill	2900/spill	93/spill
Σ^+ production	2×10^7/spill	4800/spill	370/spill

Table 5: Summary of the (π, K) trigger rate obtained from the E19 experiment and the expected trigger rate for the proposed experiment. The (π, K) trigger rate is just multiplied by the gain of the target thickness and beam intensity. The estimated numbers of the real $\Sigma^\pm$ productions are also included.

$$PIin \times Kout = (BH1 \times BH2 \times \bar{GC}) \times (TOF \times \bar{AC} \times LC). \quad (2)$$

In the E19 experiment, the $\Sigma^\pm$ data were taken using the $\pi^\pm p \to K^+\Sigma^\pm$ reactions with 1.37 GeV/c $\pi^\pm$ beams as the calibration data. We can refer to the trigger rate in the E19 beam time. The length of the LH_2 target was 13.5 cm which is almost a half of the present experiment. The beam rates were 10^6 π^-/spill and 4.3×10^5 π^+/spill, respectively. Table 5 shows the summary obtained from the E19 experiment and the expected trigger rate for the proposed experiment. The (π, K) trigger rate is just multiplied by the gain of the target thickness and the beam intensity. In the table, the estimated numbers of the real $\Sigma^\pm$ productions are also shown, which indicate that trigger rate is more than 20 times higher than the real Σ production. It is essential to make efficient trigger considering the acceptable DAQ rate of $\sim$500/spill. If needed, the fiber vertex trackers information, which will be described in the next subsection, is also used to identify the additional charged particle from the target region.

3.2 Detector system to identify the Σp scattering

Figure 16 shows a schematic view of the LH_2 target and surrounding detector system. We use a 30 cm long LH_2 target as hyperon production and hyperon proton scattering targets. The target diameter of 4$\sim$6 cm is considered, because hyperon cannot move inside the target for a long range due to its short life time. Therefore it should be comparable with the mean path length in the hyperon beam.

The LH_2 target is surrounded from inner to outer region by a scintillation fiber tracker made from 4 layers of scintillation fiber sheet, a cylindrical drift chamber and calorimeters in order to measure the trajectories of the scattered proton and the decay products from hyperon. The energy of the proton can be measured by the calorimeter.

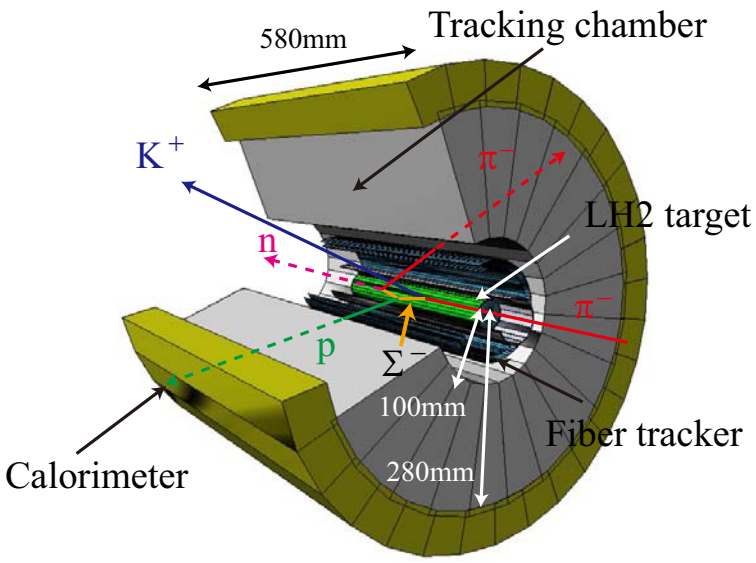

Figure 16: Schematic view of the LH_2 and surrounding detector system. The LH_2 target is surrounded by 4 layers of fiber tracker, cylindrical drift chamber and calorimeter.

3.2.1 Fiber tracker for vertex reconstruction and trigger

In realizing hyperon proton scattering with high statistics, it is essential to use high intensity π or K^- beams to produce enough hyperon beams. Accordingly, the ability to separate the real scattering events from the accidental coincidence events is necessary. Because we do not use an imaging detector, the accidental coincidence events with the Σ production might cause some errors in deriving the cross section. A good time resolution of $\sim$1 ns to separate the accidental events is required. Therefore we will install a fiber tracker at the most inner part, which also works as a vertex tracking system. The ability to trigger by the scattering events is also essential for high statistics experiment. Using the difference of the energy deposit in the fibers of π and proton, any charged particle events or proton events can be selected on the trigger level. The fiber tracker is a three dimensional tracking detector. whose odd and even layers have a u and v configuration, respectively. The cross section of the fiber is 0.5 $\times$ 1 mm^2 and the total readout channel is $\sim$1500. The each fiber signal is detected by PPD (MPPC) with a special readout board SPIROC, which enables us to read 32 ch of MPPC serially.

The SPIROC chip is an ASIC dedicated for the multi-channel PPD readout. The diagram of SPIROC board is shown in Figure 17. The SPIROC chip has 32 channel inputs of PPD and each channel has a preamplifier, slow shaper for an energy measurement, and fast shaper and discriminator for a time measurement [20]. The each discriminator output signal is sent to a FPGA control chip, then time information is obtained with a few ns resolution. By setting the threshold to the energy deposit of protons, these logic signals can also be used as a trigger.

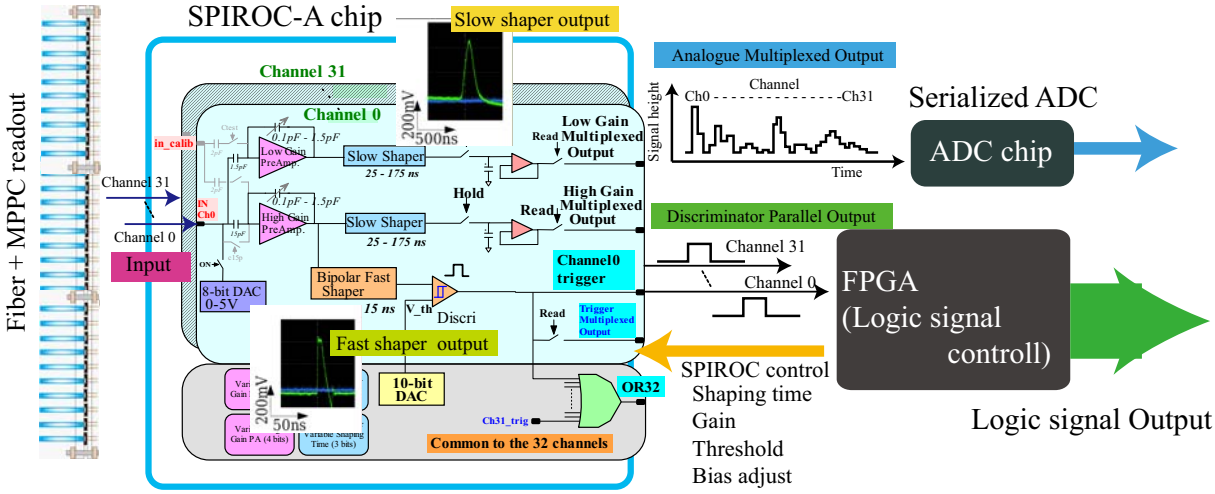

Figure 17: Diagram of the SPIROC board. The SPIROC chip has 32 channel inputs of PPD and each channel has a preamplifier, slow shaper for an energy measurement, and fast shaper and discriminator for a time measurement. The each discriminator output signal is sent to FPGA, then time information is obtained with a few ns resolution. The multiplexed analogue output is sent to external ADC chip and the digitized ADC data are read out serially.

3.2.2 Calorimeter system

The calorimeter measures the total energy of a scattered proton. We consider a plastic scintillator for the calorimeter. In order to identify the hyperon-proton scattering event, the measured energy is compared with the calculated energy from the hyperon beam momentum and the scattering angle of the proton. The resolution of the calculated energy, which is determined by the angular resolution of the scattered proton, is $\sigma = 3$ MeV. The comparable resolution is required for the calorimeter.

3.2.3 Expected performance of detector system surrounding the LH_2 target

- **Acceptance for scattered protons**

Figure 18 shows the scattering angle in the CM system of $\Sigma^- p$ system, where the open and dotted histograms show the generated distribution and the events where the scattered proton is detected, respectively. The scattering events with smaller scattering angle cannot be detected, because the energy of the corresponding proton is quite small and such proton cannot escape the target or stops at the inner fibers. Figure 19 shows the momentum and energy distributions of the scattered proton, where the hatched spectrum shows the detected events. The energy threshold of proton is ∼30 MeV. For the scattering events with a larger scattering angle, where the proton is scattered to the forward region, the detector system has a small acceptance which causes a decrease of ratio of the accepted events. The fraction of accepted and generated events is estimated to be ∼0.35.

- **Angular resolution and reconstructed energy resolution of proton**

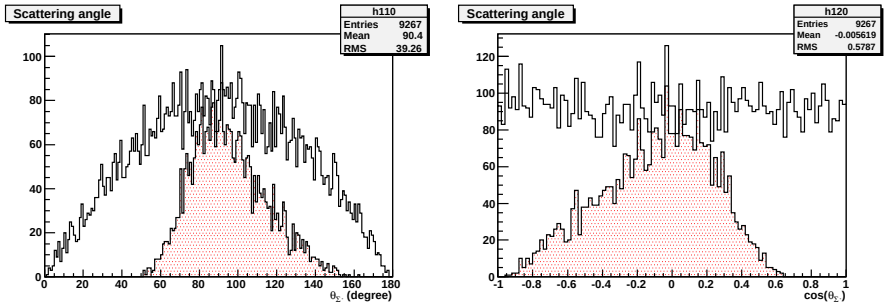

Figure 18: Scattering angle distribution of Σ^- at the center of mass system. The hatched spectrum shows the events which are detected by the detector.

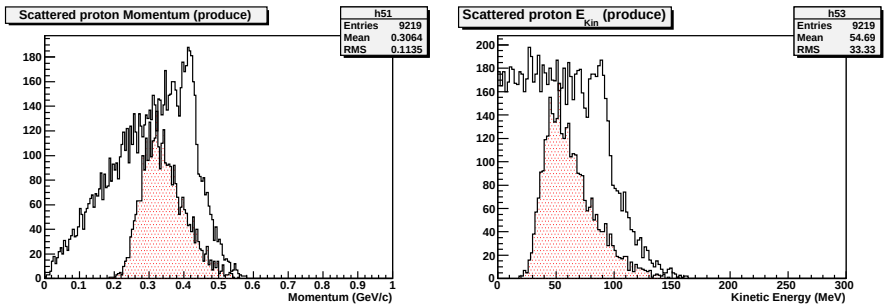

Figure 19: Momentum and kinetic energy distribution of scattered protons. The hatched spectrum shows the accepted events. The energy threshold of the kinetic energy is $\sim$30 MeV.

The scattering angle of the proton is obtained from the hyperon beam track and the proton track. Because the elastic scattering event is identified by checking the consistency between the scattering angle and the energy of the proton, the good angular resolution is required to make the S/N ratio better. Figure 20 shows the angular resolution of the scattering angle. In the simulation, we assumed that the chamber has 3 u v planes and the fiber tracker has 2 layers of u v planes. The fiber width of 1 mm is also taken into account. The angular resolution is expected to be 1.3 degree which is determined by the multiple scattering in the materials such as a target vessel, a vacuum window and fibers and so on. The resolution of the reconstructed energy of the scattered proton is estimated to be σ =3.2 MeV as shown in Figure 21.

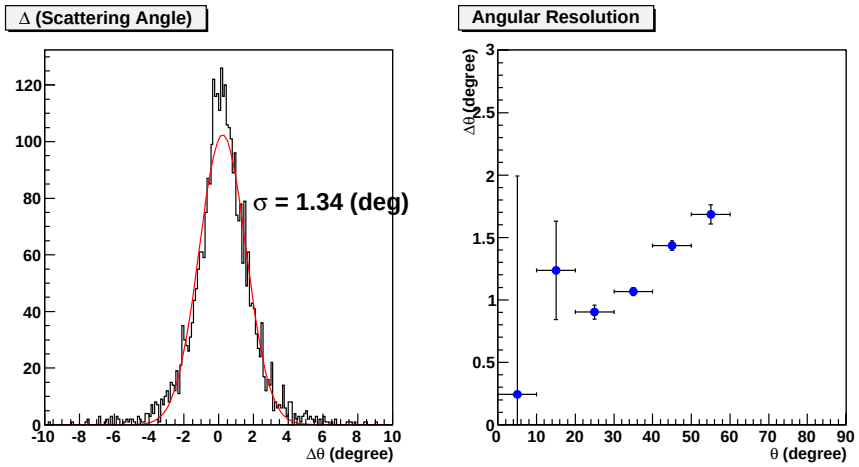

Figure 20: Angular resolution for scattered proton.

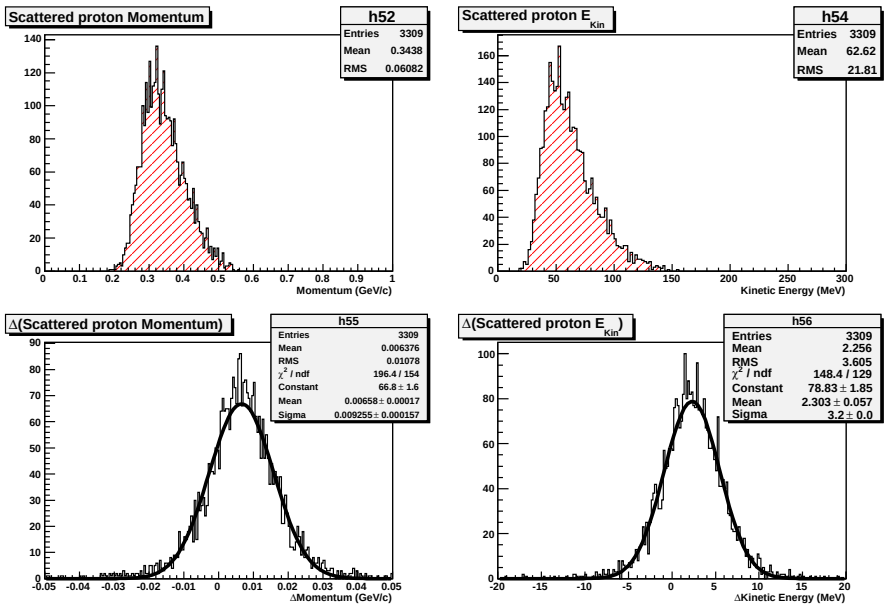

Figure 21: Momentum and kinetic energy resolution for scattered proton.

- **Vertex resolution of scattering point**

The scattering vertex is calculated as the closest distance point between tracks of hyperon beam and scattered proton. The Figure 22 shows the vertex distributions and the closest distance between these two tracks. The vertex resolution of z and x, y are calculated to be 2.0 mm and 1.0 mm, respectively, as shown in Figure 23.

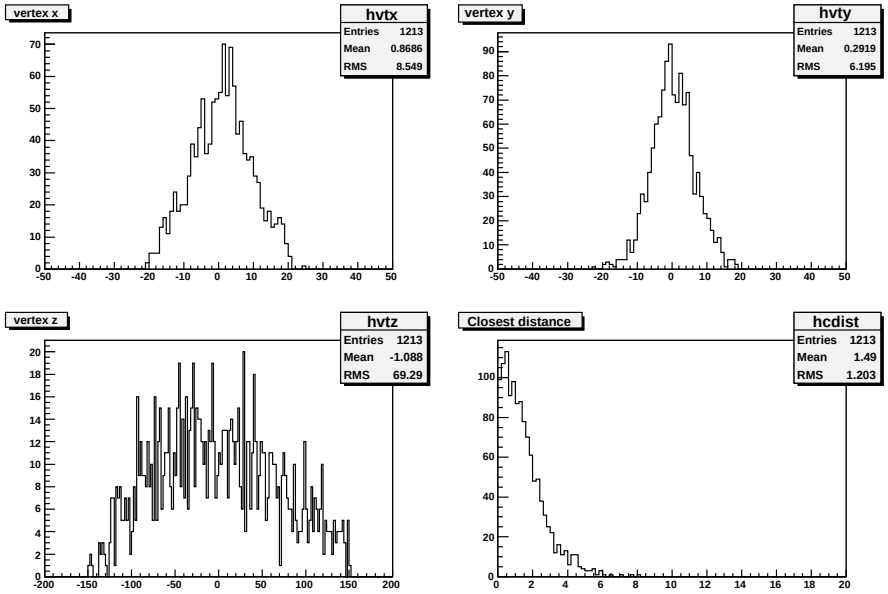

Figure 22: Vertex distribution of Σ^-p scattering point and closest distance distribution.

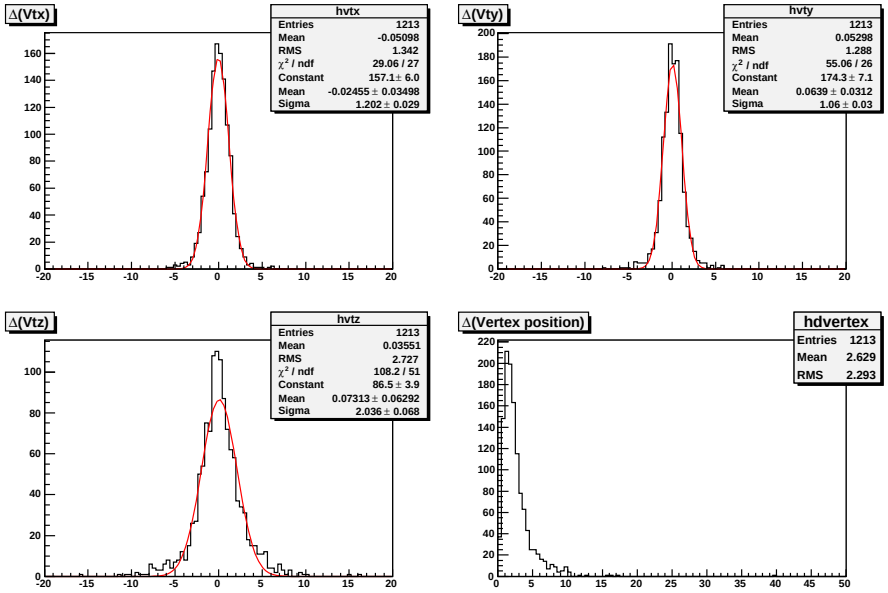

Figure 23: Resolution of Σ^-p scattering vertex.

- **Particle identification of scattering particle**

For the Σ^- production event, π^- from Σ^- decay and proton from some interactions are detected by the detector around the target. Therefore particle identification of proton and π is essential. We try to separate these particles using ΔE per unit length at fibers and total energy deposit at the calorimeter, ΔE-E method. Figure 24 shows the relation between total energy deposit per unit length at 4 fibers and the energy deposit at the calorimeter, where the red and green points represent proton and π^-, respectively. In this plot, the energy

resolution is not yet considered. There might be a contamination of the π at the high energy proton region. In order to separate π and proton without any contamination, we use other information such as the β measurement between a start counter and the calorimeter.

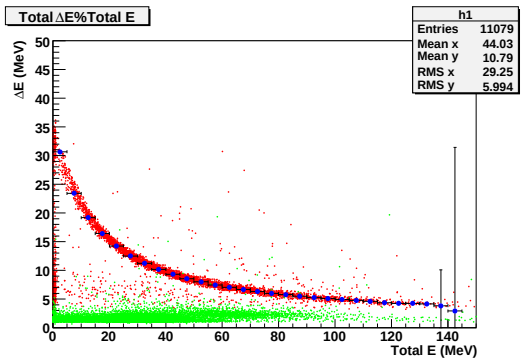

Figure 24: Relation between total ΔE per unit length at all fibers and E at the calorimeter. The red and green points represent proton and π^-, respectively.

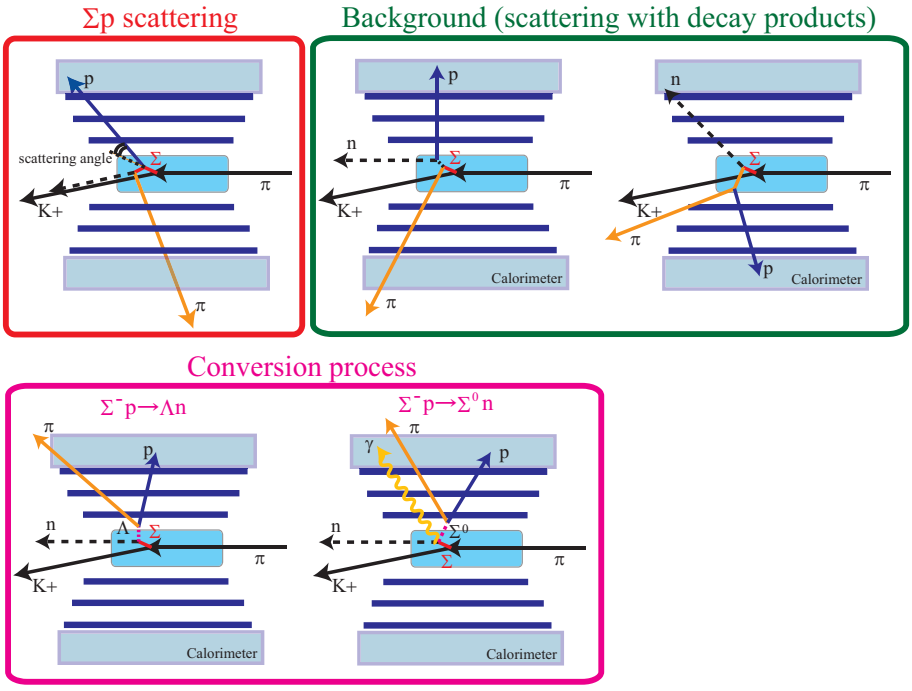

Figure 25: The background events of the $\Sigma^- p$ scattering. The main background is np and $\pi^- p$ scatterings after the Σ^- decay. The $\Sigma^- p \to \Lambda n$ conversion process, which is also one of our interesting targets, can be identified with some assumptions. However the $\Sigma^- p \to \Sigma^0 n$ conversion process can not be identified and it just makes background events.

4 Background events

We detect the scattered proton in coincidence with the Σ production. However there are background events due to the decay product of Σ hyperons. At first, in the Σ^+ case, the main background is the proton from the $\Sigma^+ \to \pi^0 p$ decay. Other background sources are protons which are scattered by the decay products from the Σ decay such as proton, neutron, and $\pi^\pm$. For the $\Sigma^- p$ reaction, the conversion processes such as $\Sigma^- p \to \Lambda n$ and $\Sigma^- p \to \Sigma^0 n$ reactions become backgrounds for the $\Sigma^- p$ elastic scattering, although $\Sigma^- p \to \Lambda n$ is one of the interesting channel. Figure 25 and Figure 26 show the summaries of the background reactions for the $\Sigma^- p$ reaction and the $\Sigma^+ p$ reaction. In order to estimate these background levels, we performed a simulation considering the realistic cross sections and angular distributions of these background events as described below. The background cross sections are quite dependent on the momentum regions of the neutron, proton and $\pi^\pm$. Figure 27 and Figure 28 show the momentum and kinetic energy distributions of neutron and π^- from Σ^- decay. Therefore in the simulation, energy dependent cross sections are also taken into account. In this section, we describe the background level and method to identify the Σp scattering events and also to suppress background events.

4.1 Neutron-proton and proton-proton scatterings

In order to estimate the contribution from np scatterings, the realistic cross section and angular dependence should be used. We used theoretical calculation of the np scattering

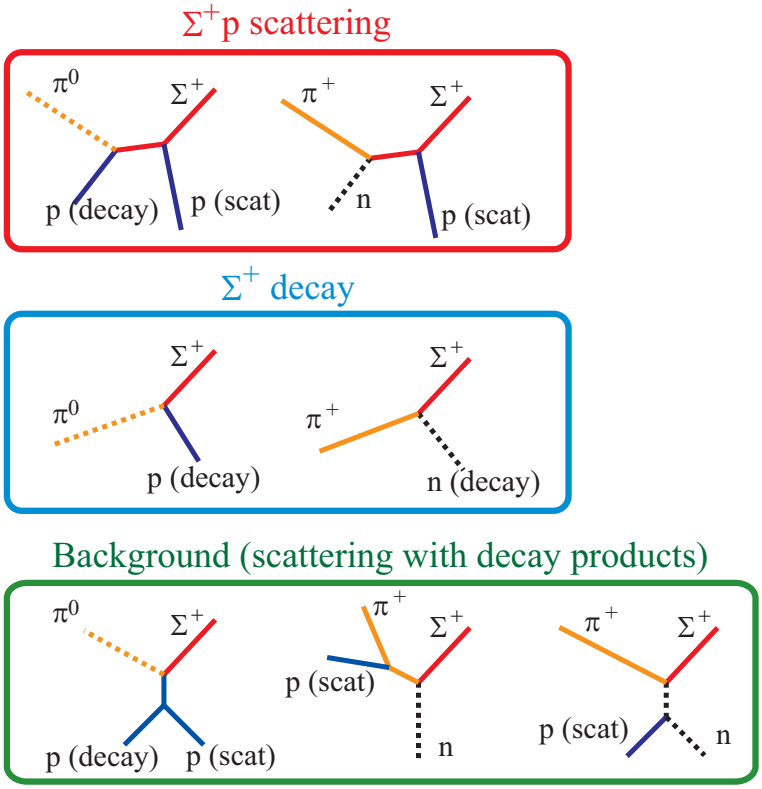

Figure 26: The background events of the $\Sigma^+ p$ scattering. Because there is a $p\pi^0$ decay channel, the proton from Σ^+ decay makes background in addition to the scattering with the decay products.

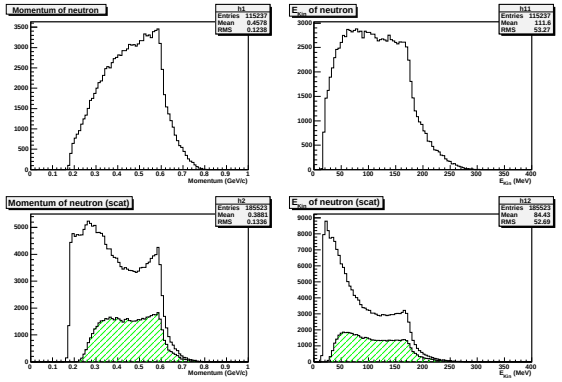

Figure 27: Momentum and kinetic energy distributions of the neutron from Σ^- decay. The bottom figures are the same distributions where the np scattering occurs. The hatched histogram shows the events where scattered proton is detected by the surrounding detector.

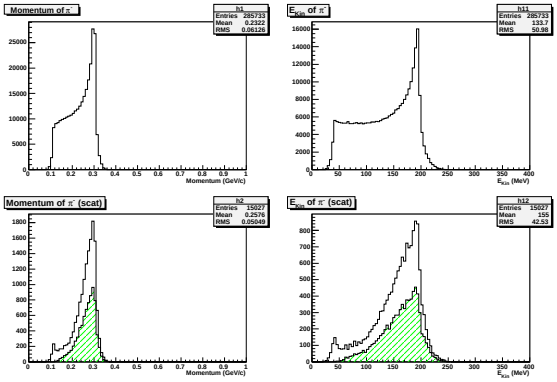

Figure 28: Momentum and kinetic energy distributions of the π^- from Σ^- decay. The bottom figures are the same distributions where π^- and proton scattering occurs. The hatched histogram shows the events where scattered proton is detected by the surrounding detector.

of the fss2 model by Fujiwara *et al.* as shown in Figure 29 [4]. For the *pp* scattering, we refereed the experimental data [21]. It is to be noticed that the cross sections increase when the energies of neutron and proton become small. In the bottom figures of Figure 27, the kinetic energy distribution of neutron which interacts proton is shown. Although number of emitted neutron from Σ decay decreases in low energy region, the number of scattered neutron increases due to the increase of the total cross section.

In the Monte Carlo simulation, both the total cross section and the differential cross section are taken into account.

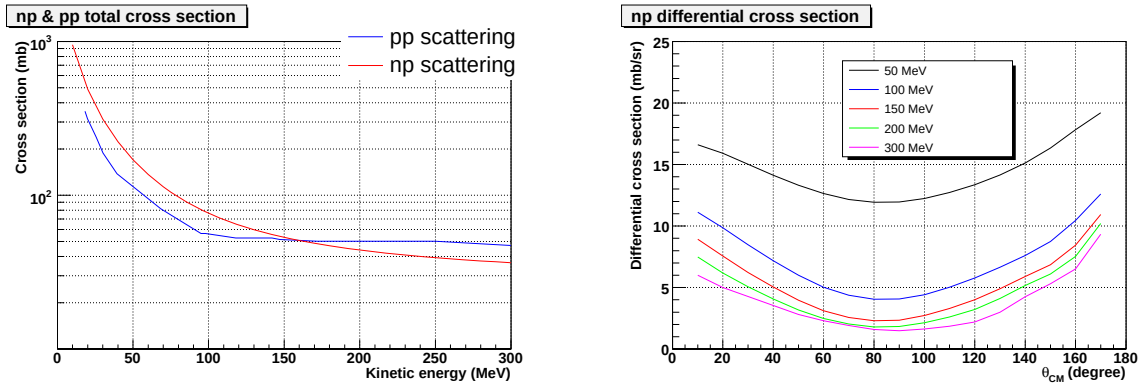

Figure 29: Total and differential cross section of *np* scattering by theoretical calculation based on fss2 model.

4.2 π^- proton and π^+ proton scatterings

Figure 30 shows the $\pi^- p$ total and elastic cross sections. The difference between total and elastic cross sections at the momentum region of $0.1 < p < 0.4$ GeV/c is understood as the contribution from a charge exchange reaction ($\pi^- p \to \pi^0 n$). Therefore we take only the contribution of the $\pi^- p$ elastic scattering into account. As the angular distribution, we use a flat distribution in the CM system. Because the cross section of the $\pi^- p$ elastic scattering is a rather small value of 20 mb, the background level of the $\pi^- p$ reaction is smaller than that of the *np* scattering.

Figure 31 shows the $\pi^+ p$ total and elastic cross sections. Compared with the $\pi^- p$ elastic scattering, the $\pi^+ p$ scattering has a larger cross section of $\sim$200 mb which is comparable with the *pp* scattering.

4.3 Background kinematics

In the event generator in the Monte Carlo simulation, we included the background processes described in the previous subsection. In order to identify the Σp scattering, we check the consistency between the hyperon beam momentum, the scattering angle and energy of the scattered proton. Here the scattering angle is defined by a crossing angle between the outgoing proton track and hyperon beam as shown in Figure 32. We also used the same scattering angle for the background events. Figure 33 shows the scattering plots between the scattering angle and the momentum of proton. For the $\Sigma^- p$ elastic scattering event, there is a reasonable correlation between the angle and the momentum, while there are broad

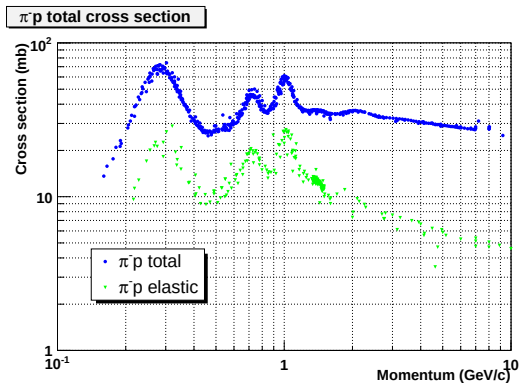

Figure 30: π^-p total cross section and elastic cross section.

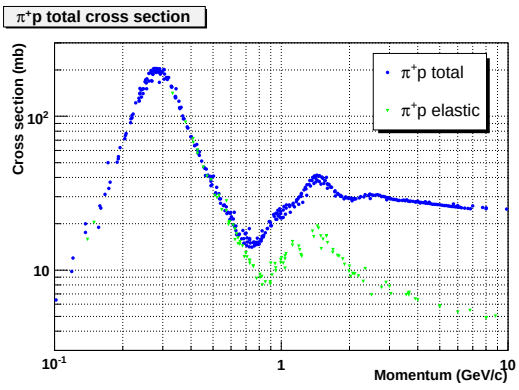

Figure 31: π^+p total cross section and elastic cross section.

distributions due to the background events. In the right figure (Σ^+p channel) of Figure 33, there is also a band of the Σ^+ decay. Unfortunately, there are overlap region between them. In order to separate from these backgrounds, good angular resolution and good energy resolution are essential.

Here we define the following values,

- $E_{measure}$: measured kinetic energy of the proton by the calorimeter,
- $E_{calculate}$: calculated kinetic energy from the hyperon beam momentum and the scattering angle,
- ΔE : difference between $E_{measure}$ and $E_{calculate}$, ($\Delta E = E_{measure} - E_{calculate}$).

For the Σp scattering event, the ΔE should be zero, although the ΔE has a broad distribution for the background events. Figure 34 shows the ΔE distribution for the Σ^- beam events, where the peak around $\Delta E = 0$ MeV and broad structures correspond to the $\Sigma^- p$ elastic scattering events and background events, respectively. The total cross section of the $\Sigma^- p$ elastic scattering is assumed to be 30 mb. Because the cross sections of the background reactions are also taken into account, the S/N ratio is reliable.

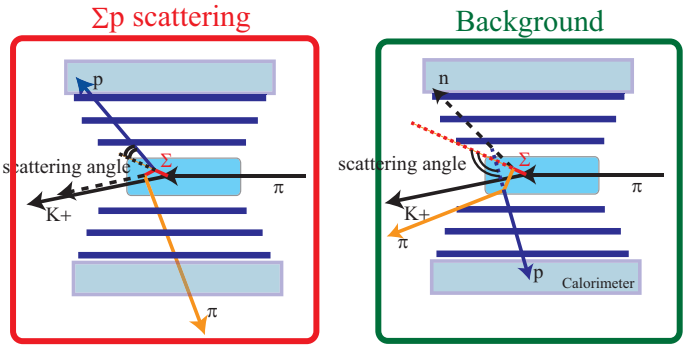

Figure 32: Definition of the scattering angle. The angle is defined as the crossing angle between the hyperon beam track and the outgoing proton.

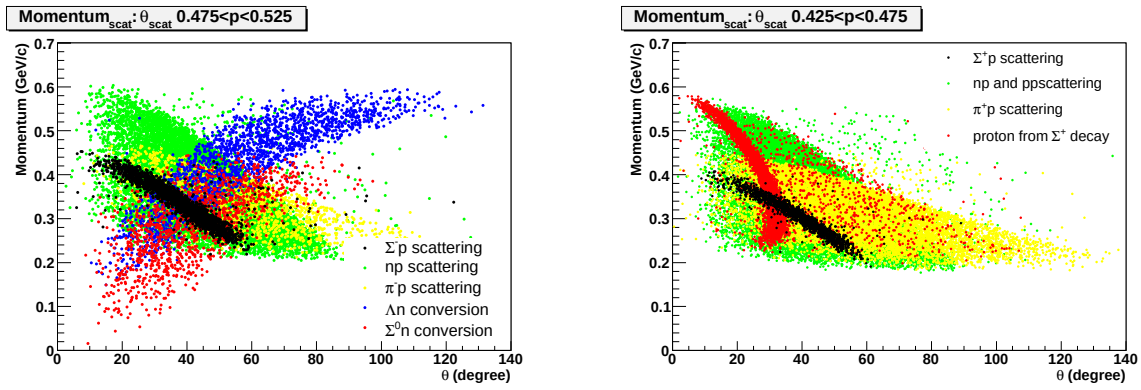

Figure 33: Relation between the scattering angle and the momentum of the scattered proton for the $\Sigma^- p$ event (left figure) and the $\Sigma^+ p$ event (right figure) with background events. The scattering angle is defined by the cross angle by a hyperon beam track and a outgoing proton.

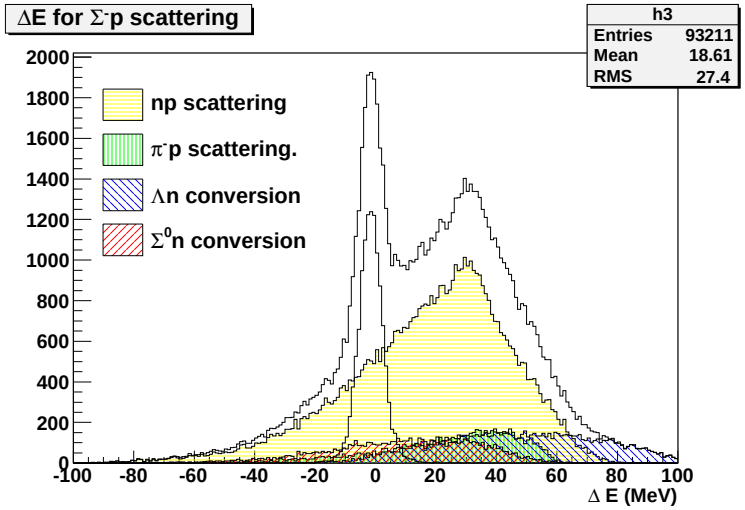

Figure 34: Difference between the calculated kinetic energy from the scattering angle and measured kinetic energy. The peak structure around ΔE=0 MeV corresponds to the Σ^-p scattering. The green and yellow hatched spectra show the background due to the np and $\pi^- p$ scatterings, respectively. The blue and read hatched spectra show the conversion process of $\Sigma^- p \to \Lambda n$ and $\Sigma^- p \to \Sigma^0 n$, respectively.

4.3.1 Background suppression

In the ΔE distribution of Figure 34, there is a large background below the $\Sigma^- p$ scattering events. Therefore the suppression of the background events is essential.

At first, we check the closest distance between the hyperon beam and the outgoing proton. Figure 35 shows the closest distance distribution. For the scattering event, this closest distance concentrates around zero as shown by the blue histogram in Figure 35, while in the background events, it shows a broad distribution. When the closest distance is required to be less than 5 mm, $\sim$45 % of background events are suppressed and the survival ratio for the signal event is 97%.

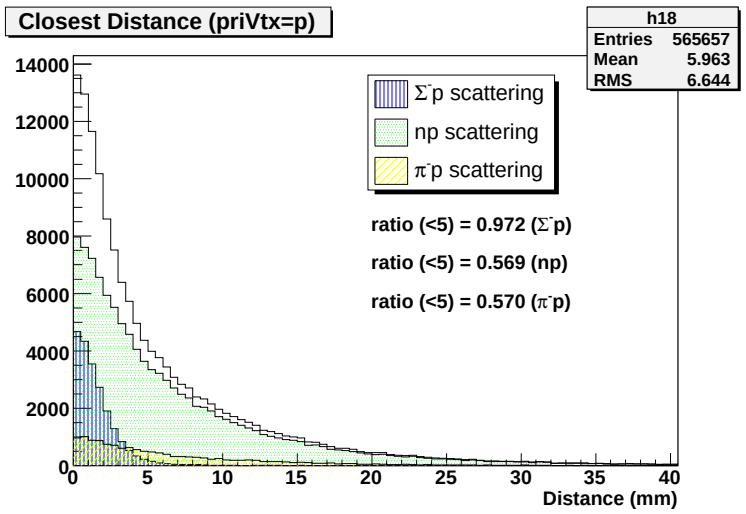

Figure 35: Closest distance distribution for each reaction. The number shows the survival ratio when we set cut value at 5 mm.

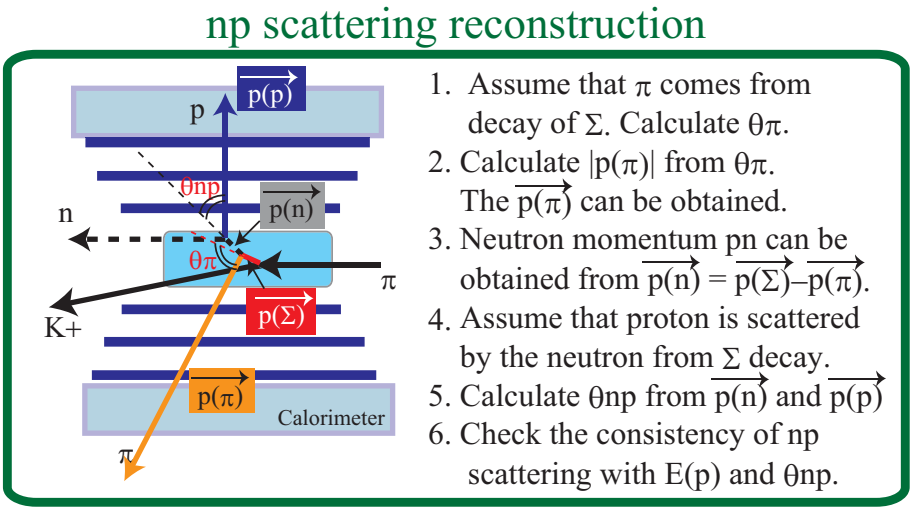

Figure 36: Reconstruction procedure of *np* scattering events.

As the second method to suppress more background, we detect and analyse a π^- particle from the Σ^- decay and reconstruct the *np* scattering background as explained in Figure 36. The detector system around the LH_2 target has a large acceptance of $\sim$79 % for π from the Σ^- decay. By using the information of the π^-, we try to suppress the background event due to the *np* scattering. When we obtain the momentum of the π^-, the momentum of the neutron from the Σ decay can be obtained assuming the Σ decay kinematics. It is difficult to measure the kinetic energy of π^-. However by measuring the trajectory of π^-, the momentum can be obtained using the assumption. The emission angle of the π^- from the Σ^- beam can be measured using the Σ^- beam direction and the direction of the π^-. If we assume that the π^- comes from the Σ^- decay, the momentum of the π^- can be obtained using the momentum of the Σ^- beam and the emission angle (θ_π). Then the neutron momentum can be obtained by $\vec{p}(n) = \vec{p}(\Sigma^-) - \vec{p}(\pi^-)$. The momentum of the neutron can be calculated

with an accuracy of 1.8 MeV/c.

Next, we assume that an outgoing proton is scattered by the neutron from the Σ^- decay. We check the consistency between the scattering angle (θ_{np}) between the outgoing proton and the neutron and kinetic energy of the proton. Figure 37 shows the difference between the measured energy of the proton and the calculated energy with the assumption of the np scattering, where the np scattering event shows the peak around $\Delta E = 0$ MeV, although other reactions show broad distributions. If we reject events of -8 $< \Delta E <$ 8 (MeV), the np scattering events are suppressed to $\sim$70%, although about 10% of the Σ^-p scattering is also removed.

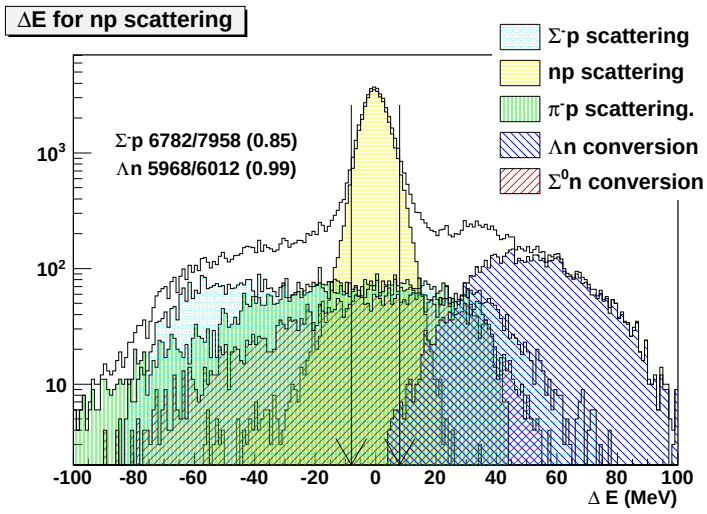

Figure 37: Difference between the measured energy of the proton and the calculated energy with the assumption that the proton is scattered by the neutron from the Σ^- decay. The np scattering event shows the peak around $\Delta E = 0$ MeV, although other reactions show broad distributions.

5 Analysis and the expected results

In this section, we present the expected results using the 16×10^6 tagged Σ^- beam and the 55×10^6 tagged Σ^+ beam. The procedures to select the scattering events and to derive the cross sections are described in detail.

5.1 Event selections of $\Sigma^- p$ elastic scattering and $\Sigma^- p \to \Lambda n$ inelastic scattering

In the Σ^- beam experiment, there are five possible reactions where a proton is emitted in coincidence with the Σ^- production, as shown in Figure 25, namely the $\Sigma^- p$ elastic scattering, Λn inelastic scattering, $\Sigma^0 n$ inelastic scattering, np scattering and $\pi^- p$ scattering. In these reactions, the $\Sigma^- p$ elastic scattering can be identified by detecting the scattered proton. By detecting the π^- from the Σ^- decay, the np scattering and Λn inelastic scattering can be identified with some assumptions as explained in the previous section. The procedure to identify the Λn inelastic scattering is shown in Figure 38, where the π^- and proton are assumed to be the decay product of Λ.

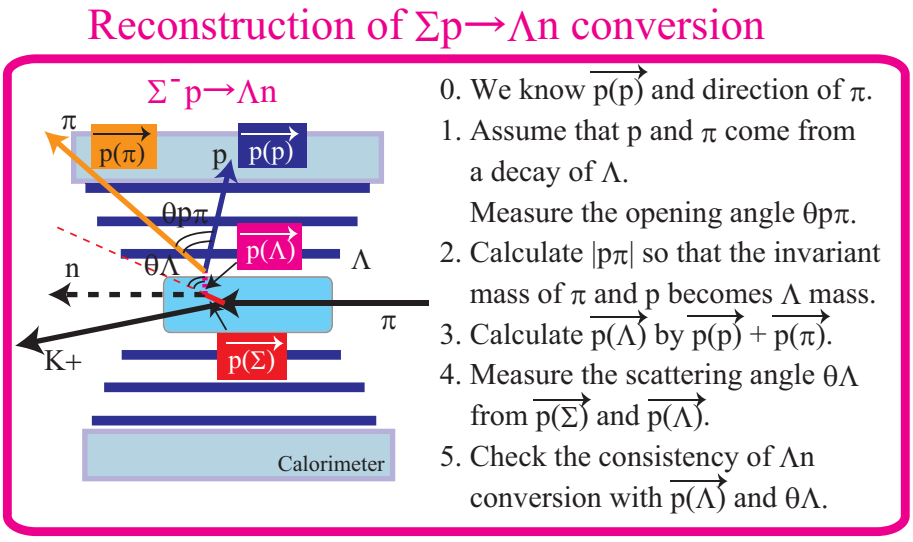

Figure 38: Reconstruction procedure of the Λn conversion process.

In the analysis, we make three ΔE (Δp for Λn reaction) distributions assuming the following three reactions, $\Sigma^- p$ elastic scattering, $\Sigma^- p \to \Lambda n$ inelastic scattering and np scattering, as shown in Figure 39. For each assumption, there is a peak around $\Delta E = 0$ which corresponds to the assumed reaction and a broad structure due to other reactions. In order to improve the S/N ratio for the $\Sigma^- p$ and Λn reactions, the following cuts are applied.

- The closest distance cut as shown in Figure 35 for the $\Sigma^- p$ scattering. For the Λn conversion event, we check the closest distance between π^- and proton.
- The np scattering cut. The event of -8 $< \Delta E_{np}$ (MeV) $<$ 8 is removed as the np scattering events. The survival ratios of the $\Sigma^- p$ and Λn reactions are estimated to be $\sim$85% and $\sim$99%, respectively.

- The Λn conversion cut for the $\Sigma^- p$ scattering event. The events of $-0.05 < \Delta p$ (GeV/c) < 0.1 are rejected as the Λn conversion events.

- The $\Sigma^- p$ scattering cut for the Λn conversion event. The events of $-10 < \Delta E$ (MeV) < 10 are rejected as the $\Sigma^- p$ scattering events.

Figure 40 shows the ΔE distribution after these background suppression cuts. The Λn scattering process is almost background free due to the Q value at the Λ decay. For the $\Sigma^- p$ scattering, although the S/N ratio is much improved, there exists the unavoidable background. When the differential cross section is derived, the contribution from the background should be subtracted.

The number of the $\Sigma^- p$ scattering events is estimated to be 9,500 for the 16×10^6 tagged Σ^- beam assuming that the total cross section of the $\Sigma^- p$ scattering is 30 mb and the angular distribution is flat. The Λn conversion is expected to be 6,000 events with the same assumption, that is, the conversion cross section is 30 mb.

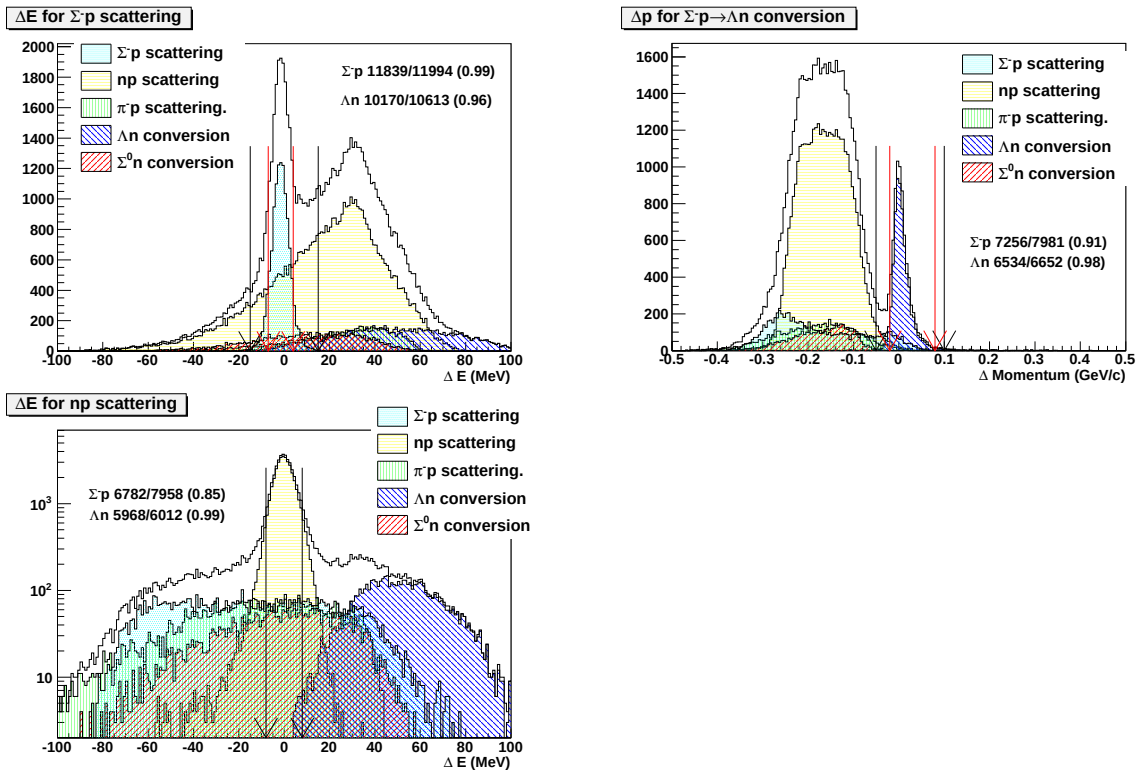

Figure 39: ΔE distributions for $\Sigma^- p$ (Left-Up) and np scatterings (Right-Up) and Δp distribution for $\Sigma^- p \to \Lambda n$ conversion reaction (Left-Down). For the $\Sigma^- p$ scattering event, ΔE distribution makes a peak around $\Delta E = 0$, although other reactions makes the broad distributions. This relation is the same for other reactions.

5.2 Event selection of $\Sigma^+ p$ elastic scattering

The $\Sigma^+ p$ scattering experiment is more challenging than the $\Sigma^- p$ scattering experiment due to the following reasons. At first, the lifetime of the Σ^+ is half of that of Σ^- because there

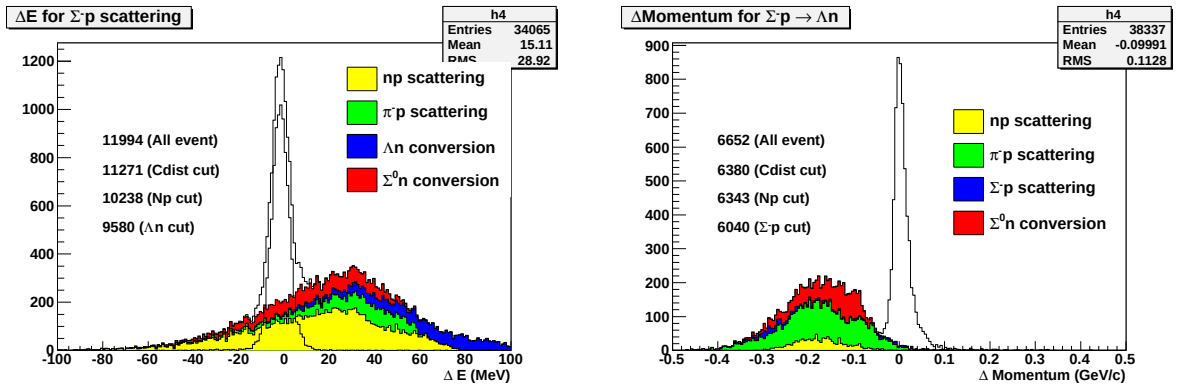

Figure 40: ΔE distribution for the $\Sigma^- p$ reaction (Left) and Δp distribution for the $\Sigma^- p \to \Lambda n$ conversion reaction (Right) after the background suppression. The numbers in the histograms represent the survival event number after each cut. It is remarking that the Λn conversion process is almost background free.

are two decay modes, $\Sigma^+ \to p\pi^0$ and $\Sigma^+ \to n\pi^+$. The scattering probability becomes about half of the $\Sigma^- p$ scattering. The second point is the background level, in particular from protons associated with the Σ^+ decay, which is absent in the $\Sigma^- p$ scattering. In addition the scattering with the decay products contributes to the background. The background cross section of the π^+ is also 10 times larger than the $\pi^- p$ cross section as shown in Figure 31.

Figure 41 shows the ΔE distributions of the assumed $\Sigma^+ p$ scattering, where left and right figures are for the $\Sigma^+ \to p\pi^0$ decay mode and the $\Sigma^+ \to n\pi^+$ decay mode, respectively. In the left figure of the $\Sigma^+ \to p\pi^0$ mode, the background distribution due to the Σ^+ decay is scaled to 1/100. Therefore, if we detect only single proton, almost all protons are from the Σ^+ decay. In order to suppress the contribution of the $\Sigma^+ \to p\pi^0$ decay, it is indispensable to detect two particles, namely the scattered proton and other charged particle from the Σ^+.

In order to improve the S/N ratio, the following cuts are applied which is almost the same technique used for the $\Sigma^- p$ scattering.

- Two-particle detection is required in order to suppress the Σ^+ decay events. The two-proton detection probability is roughly 13% for the $\Sigma^+ p$ scattering. For the $n\pi^+$ decay mode, the detection probability for the scattered proton and the π^+ is about 22%.
- The closest distance cut between the Σ^+ beam and the scattered proton. Figure 42 shows the closest distance distributions for two decay modes.
- The np scattering cut is also applied for the $n\pi^+$ decay mode. Figure 43 shows the ΔE distribution of the np scattering.

Figure 44 shows the ΔE distributions after the above suppression cuts. In the $p\pi^0$ decay mode, by selecting two proton events, the background due to the decay can be removed almost completely. Because, for the pp event, the energy of proton from the Σ^+ decay is divided by two protons, the probability for two protons to escape from the target is small. On the other hand, in the $\Sigma^+ p$ scattering events, the proton from the decay has a higher energy thanks to the Q value of the decay. Therefore the two proton detection probability is rather high and this makes the S/N ratio better. For the $\pi^+ n$ decay mode, the np scattering

can be suppressed, while the $\pi^+ p$ scattering events can not be suppressed that causes the unremovable background.

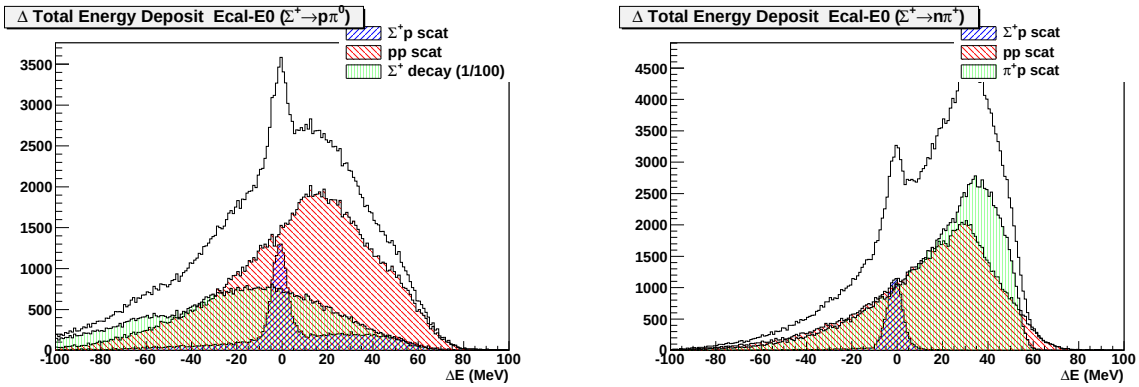

Figure 41: ΔE distributions for $\Sigma^+ p$ scattering assumption. The left figure shows the ΔE distribution for the $\Sigma^+ \to p\pi^0$ decay mode. The right figure shows the ΔE distribution for the $\Sigma^+ \to n\pi^+$ decay mode. In the left figure of the $\Sigma^+ \to p\pi^0$ mode, the background distribution due to the Σ^+ decay is scaled to 1/100.

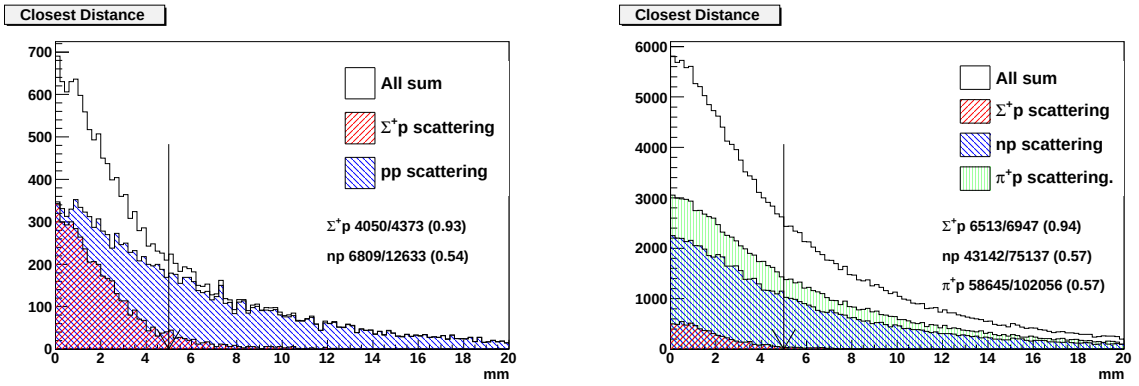

Figure 42: The closest distance distribution between the Σ^+ beam and the scattered proton for the $p\pi^0$ decay mode (left) and $n\pi^+$ decay mode.

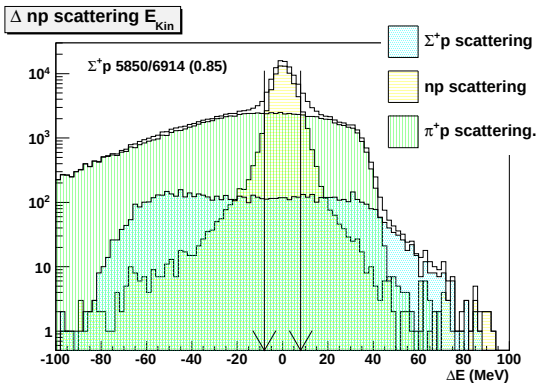

Figure 43: The ΔE distribution with assumption of the np scattering.

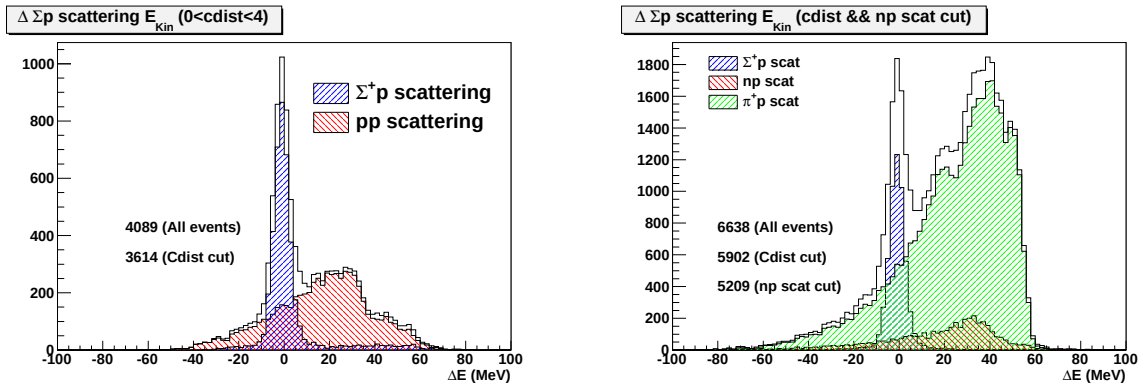

Figure 44: The ΔE distributions after the background suppression cut for the $p\pi^0$ decay mode (left) and the $n\pi^+$ decay mode (right). By selecting two proton events, the background due to the decay can be removed almost completely. For the $\pi^+ n$ decay mode, the np scattering can be suppressed. However the $\pi^+ p$ scattering events can not be suppressed in the present method. There exists the background due to the $\pi^+ p$ reaction.

5.3 Differential cross section

We calculate the differential cross section from the number of detected Σp scattering events and the track length of Σ beam in the LH_2 target. The differential cross section is defined by the following equation,

$$\frac{d\sigma}{d\Omega}(cos\theta, p) = \frac{\Sigma_i (N_{scat,i}(cos\theta, p)/\epsilon_i(cos\theta, vertex))/\epsilon_{ana}}{L_{beam}(cos\theta, p) \cdot \rho_{LH2} \cdot d\Omega}. \tag{3}$$

The ϵ_i is the efficiency to detect the i-th scattered proton. This depends on the scattering angle and the scattering point. Therefore, this efficiency correction is applied event by event. The $L_{beam}(cos\theta, p)$ is the track length in the LH_2 target region where a reasonable acceptance is obtained. This is explained in detail in Section 5.6. The ϵ_{ana} represents the efficiency of analysis cut such as the closest distant cut and so on.

cut	$\Sigma^- p$ scattering	Λn conversion
Closest distance cut	0.94	0.96
np scattering cut	0.91	0.99
Λn conversion cut	0.94	–
$\Sigma^- p$ scattering cut	–	0.95
total	0.80	0.90
cut	$\Sigma^+ p$ scattering ($p\pi^0$ decay)	$\Sigma^+ p$ scattering ($n\pi^+$ decay)
Closest distance cut	0.88	0.88
np scattering cut	–	0.88
total	0.88	0.77

Table 6: Summary of the each cut efficiency.

5.4 Cut efficiencies

Table 6 shows the summary of the cut efficiencies.

5.5 Efficiency to detect the scattered proton

The efficiency of detecting the scattered proton depends on the reaction position, momentum of the proton and scattering angle. We estimate this efficiency event by event with a Monte Carlo simulation. Figure 45 shows a schematic view of $\Sigma^- p$ scattering. The reaction point, scattering angle (θ) and momentum of proton can be obtained from the detector information. The azimuthal angle (ϕ) along the Σ^- is a free parameter. In the simulation, we generate proton with the detected momentum from the detected point. For θ, the obtained value is used. The ϕ is the free parameter and is generated uniformly from 0 to 360 degree. Then the efficiency is obtained as the ratio of the detected proton number to the generated proton number (the generated number is 1000 for each event).

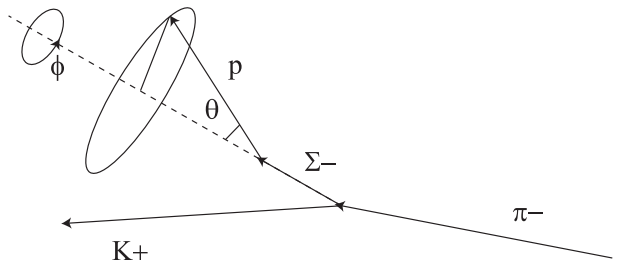

Figure 45: Schematic view of $\Sigma^- p$ scattering.

5.6 Σ track length considering the detector acceptance

We estimate the track length of the $\Sigma^\pm$ beams in the LH_2 target. We do not know the track length event by event, because the decay point of the Σ is not detected. However, because we measure the primary vertex point and the Σ beam momentum as the missing momentum of the $\pi p \to K^+ X$ reaction, we can estimate the total track length using a Monte Carlo

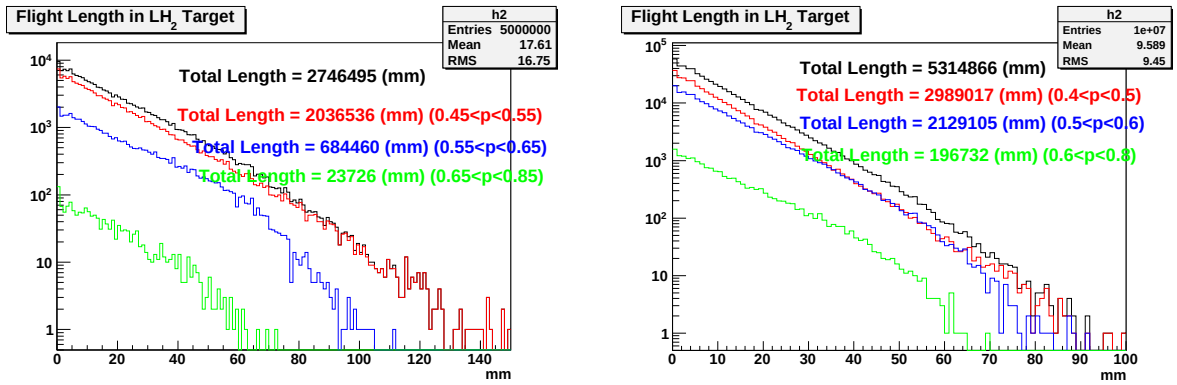

Figure 46: Estimated flight length distribution for three different momentum ranges by the Monte Carlo simulation using the information of the primary vertex and the momentum obtained from the spectrometer analysis. The sum of the flight length is the total track length which is written as "Total Length".

simulation using the measured information. Figure 46 shows the estimated flight length distribution for three momentum regions.

We have to consider the detector acceptance as a function of the primary vertex point (z, beam direction). For the forward going proton ($\cos\theta \sim -1$), detection ratio decreases at the downstream primary vertex region, because there is no detector acceptance as shown in Figure 47. Therefore, if we use the same track length for all scattering angle range, the differential cross section at $\cos\theta \sim -1$ might be underestimated. Figure 48 shows the primary vertex distribution for each scattering angle, where the open and red hatched histograms show the generated scattering point and the detected scattering point, respectively. For each scattering angle range, we set the acceptable primary vertex region as shown by the blue lines where the detector acceptance is reasonable. When the differential cross section is derived, we use the total track length within the acceptable region for each $\cos\theta$ region ($L_{beam}(cos\theta, p)$). In order to count the scattering number ($N_{scat,i}(cos\theta, p)$), the primary vertex point is required to be within the region.

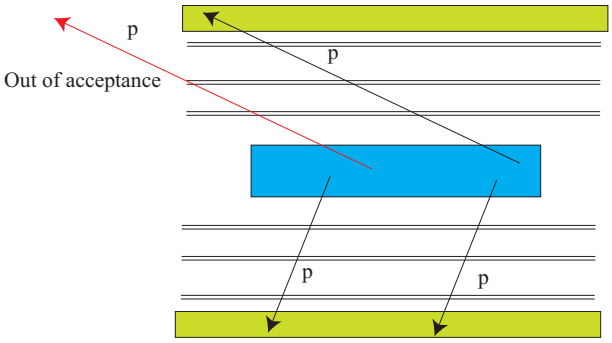

Figure 47: Schematic view of the detector acceptance. The detector acceptance depends on the primary vertex and scattering angle.

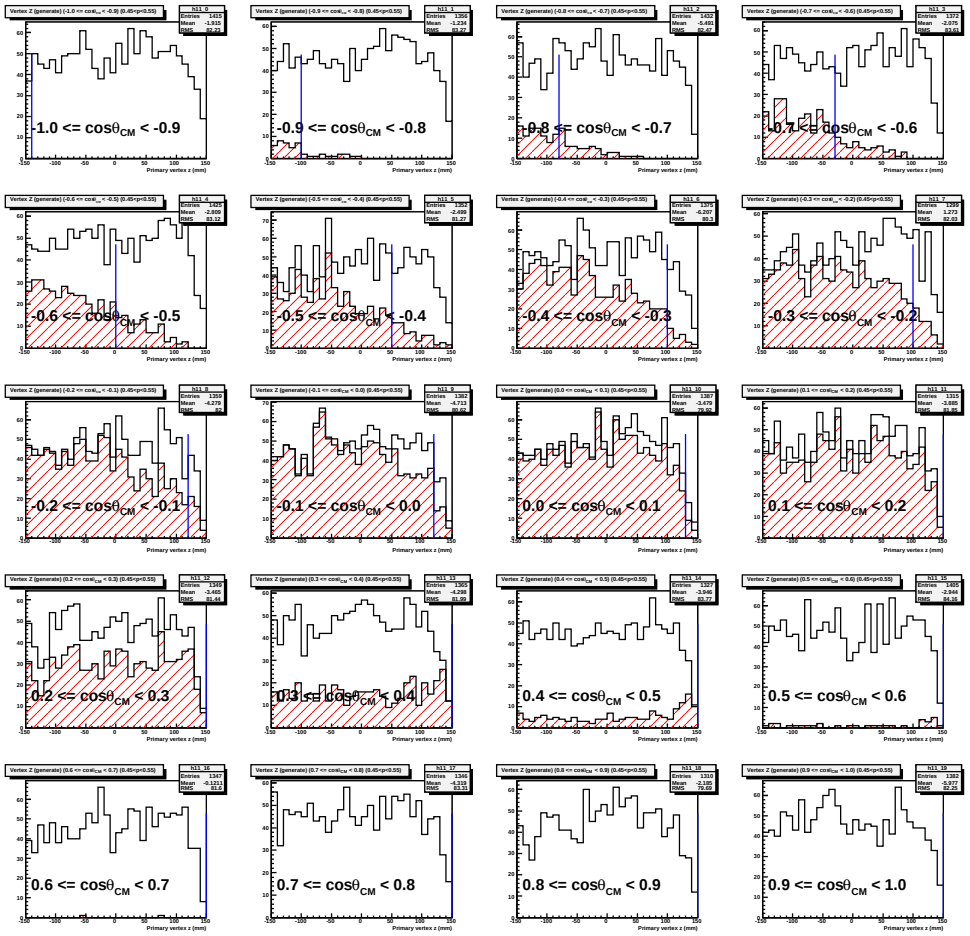

Figure 48: Primary vertex distribution for each scattering angle for the data of $0.45 < p_\Sigma(\mathrm{GeV}/c) < 0.55$. The open histogram shows the generated distribution. The red histogram shows the primary vertex distribution when the proton scattered to the each angle is detected. For the backword scattering events around $cos\theta_{CM} = -1$, the reaction point is limited to the upstream region of the target. For the forward scattering events around $cos\theta_{CM} = 1$, the kinetic energy of the proton is small and such low energy proton can not be detected.

5.7 Background subtraction

In order to identify the Σp scattering event, we apply the kinematical cut to check the energy difference between the measured proton energy and the calculated proton energy. However, there exists unremovable background as shown in Figure 40. We have to estimate the amount of the differential cross section and angular distribution due to the background. In order to estimate the background level and obtain the contribution of the real event, we make a plot of the double differential cross section $d^2\sigma/d\Omega dE$ for each scattering angle from the ΔE distribution in Figure 44. Figure 49 shows the $d^2\sigma/d\Omega dE$ distributions for the $\Sigma^- p$ reaction with the Σ^- beam momentum of $0.45 < p(\mathrm{GeV}/c) < 0.55$. The red points in Figure 49 are obtained from the events which satisfy the closest distance cut and include not only the real $\Sigma^- p$ scattering events but also the background events. In order to derive the differential cross section, we fitted the histograms by the Gauss peak for the signal and 1st

order polynomial background as shown in Figure 49. The differential cross section is obtained from the integral of the Gauss peak. The green points represent the estimated background from the large closest distance region as shown in Figure 50. This estimated background can be a reference, although, from the simulation, it is studied that the estimated background can not reproduce the background distribution of the red histogram perfectly.

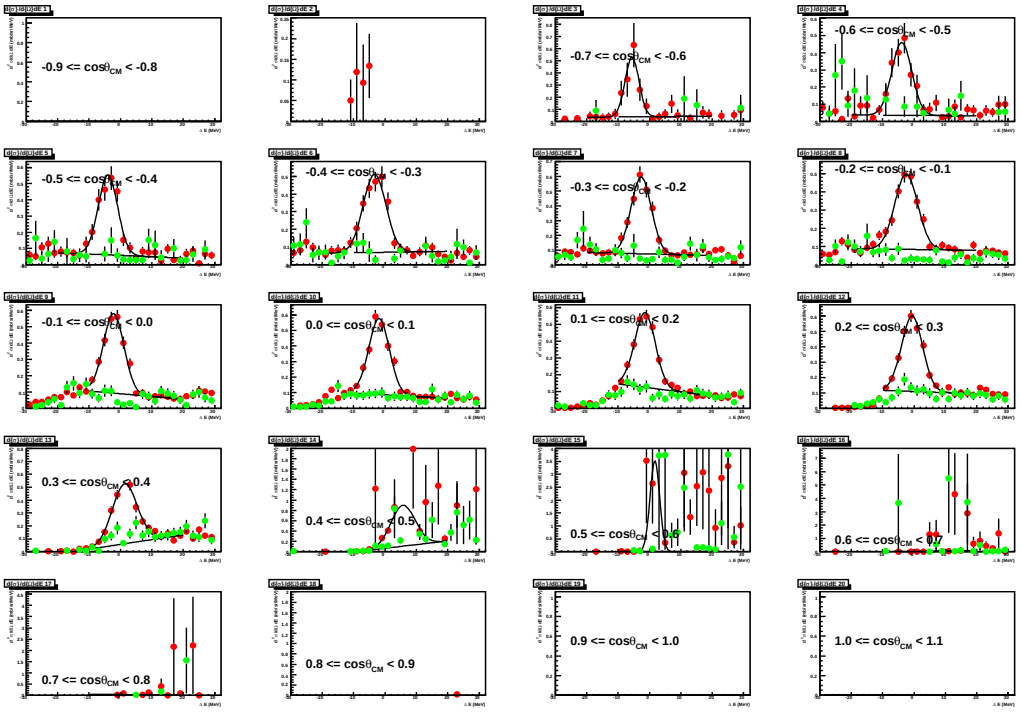

Figure 49: The double differential cross sections $d^2\sigma/d\Omega dE$ are shown for each scattering angle. The red points are obtained from the events which satisfy the closest distance cut and include not only the real $\Sigma^- p$ scattering events but also the background events. The green points represent the estimated background from the large closest distance region. The black lines (signal+background and only background) show the fit results assuming the Gauss peak and 1st order polynomial background.

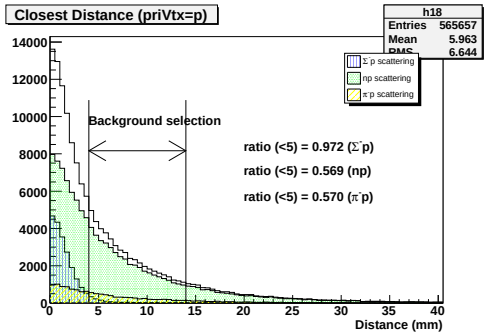

Figure 50: Background selection using the large closest distance region. The green plot in 49 shows the contribution of events from this region.

5.8 Differential cross section of the $\Sigma^- p$ elastic scattering

We derive the $\Sigma^- p$ differential cross section. The data set is generated from 16×10^6 Σ^- beam and the total cross section is assumed to be 30 mb with a flat angular distribution, i.e. 2.4 mb/sr. Histograms in Figure 51 show the obtained differential cross sections for the two momentum regions. The obtained spectra show the flat distribution for the reasonable acceptance region. The absolute value is still different, and we need further detailed study. However, in the proposed experiment, the differential cross section can be measured with much better accuracy.

In the figures, the two theoretical calculations, the Nijmegen model and the Quark Cluster model, are also shown. In this reaction, there is no large difference between the two theoretical predictions. In order to test the theoretical framework, we have to provide good statistics data which constraint the angular dependence of the theoretical predictions. The expected results can be a constraint for the theoretical models.

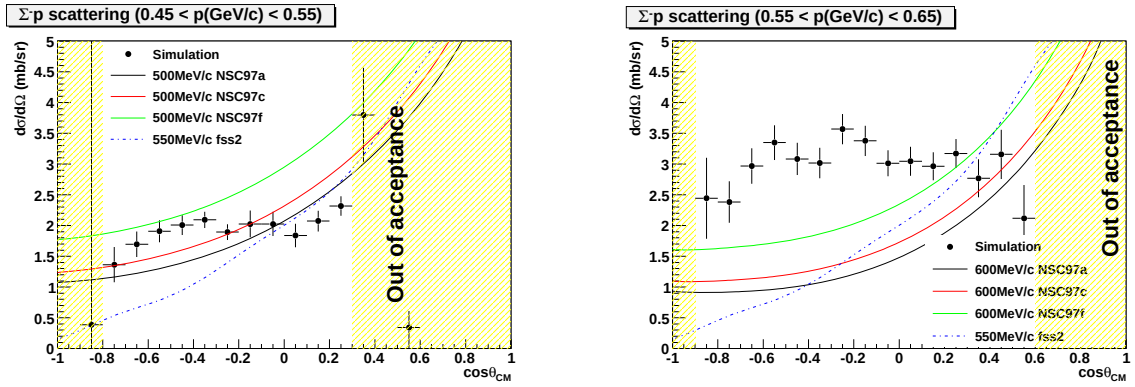

Figure 51: The expected differential cross section of the $\Sigma^- p$ scattering in the beam momentum regions of $0.45 < p$ (GeV/c) < 0.55 (left) and of $0.55 < p$ (GeV/c) < 0.65 (left). The differential cross section is the obtained from the integral of the Gauss peak of the $d^2\sigma/d\Omega dE$. The yellow hatched region shows the region out of acceptance. Theoretical predictions by the OBEP (Nijmegen Soft Core) models and the quark cluster (RGM FSS) models are shown together.

5.9 Differential cross section of the $\Sigma^- p \to \Lambda n$ inelastic scattering

Figure 52 shows the obtained differential cross section in the same condition with the $\Sigma^- p$ scattering. The histograms show the results with the 16×10^6 tagged Σ^- beam. In the $\Sigma^- p \to \Lambda n$ reaction, the background contamination is quite small because the energy of the proton from the Λ decay has a rather high energy due to the Q value at the decay and kinematics is separated from other reactions. The data with a wide scattering angle can also be taken.

In the figures, the two theoretical calculations, the Nijmegen model and the Quark Cluster model, are also shown. The tendency of the angular dependence is similar for the two predictions although behaviour around $\cos\theta > 0.2$ is different. The data of the $\Sigma^- p \to \Lambda n$ reaction enable us to test the theoretical model for the wide scattering angle for the first time in the YN scattering.

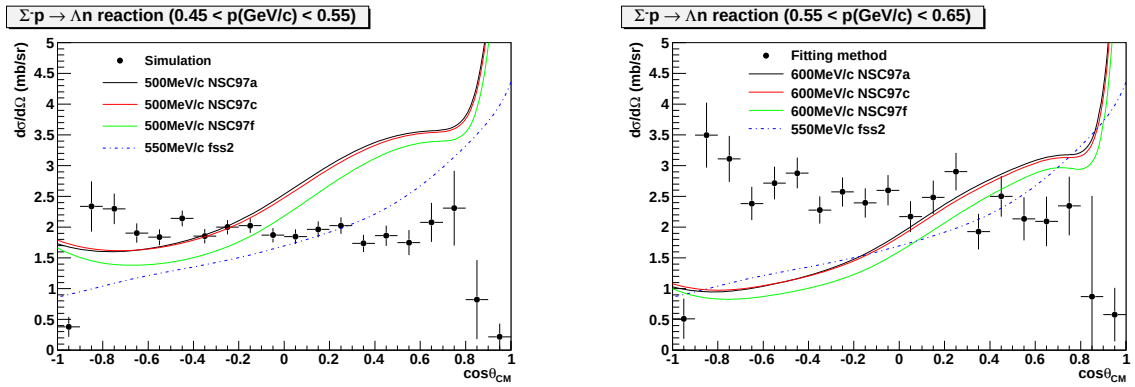

Figure 52: Differential cross section of the $\Sigma^- p \to \Lambda n$ inelastic scattering in the beam momentum regions of $0.45 < p\ (\mathrm{GeV}/c) < 0.55$ (left) and of $0.55 < p\ (\mathrm{GeV}/c) < 0.65$ (left). Theoretical predictions by the OBEP (Nijmegen Soft Core) models and the quark cluster (RGM FSS) models are shown together.

5.10 Differential cross section of the $\Sigma^+ p$ elastic scattering

The differential cross section of the $\Sigma^+ p$ scattering is also derived using the simulated data of 55×10^6 tagged Σ^+ beam. Figure 53 and Figure 54 show the obtained spectra for the $\Sigma^+ \to p\pi^0$ and the $\Sigma^+ \to n\pi^+$ decay modes, respectively. Because the background contributions for the two decay modes are different, the cross sections are derived separately for each channel.

In this channel, the theoretical prediction is very different due to the treatment of the repulsive core. The Quark Cluster model predicts about twice larger cross section than that of the Nijmegen model. The goal of investigating the $\Sigma^+ p$ channel is to test the theoretical models and to confirm the effect of the quark Pauli effect by providing a good statistics data. The expected spectrum fulfills this goal and enables us to confirm the magnitude of effects brought by the repulsive core.

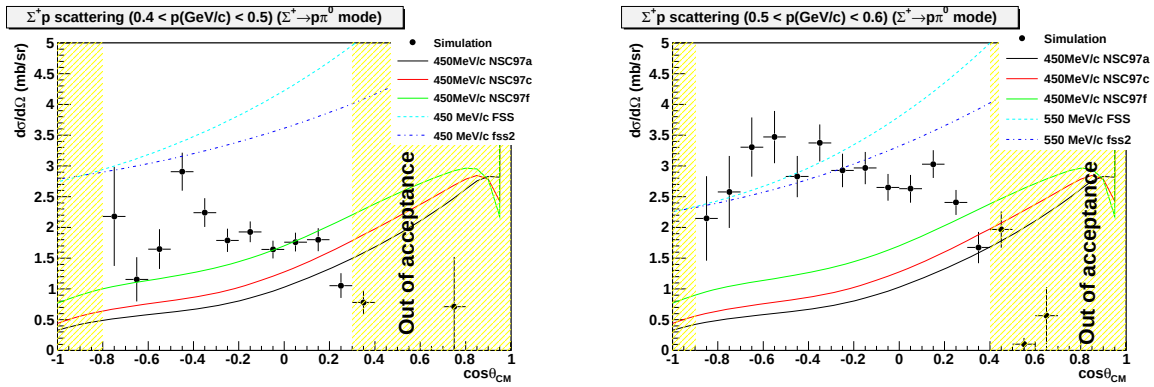

Figure 53: Differential cross section of the $\Sigma^+ p$ elastic scattering in the beam momentum regions of $0.4 < p$ (GeV/c) < 0.5 (left) and of $0.5 < p$ (GeV/c) < 0.6 (left) for the $\Sigma^+ \to p\pi^0$ decay mode. The yellow hatched region shows the region out of acceptance. Theoretical predictions by the OBEP (Nijmegen Soft Core) models and the quark cluster (RGM FSS) models are shown together.

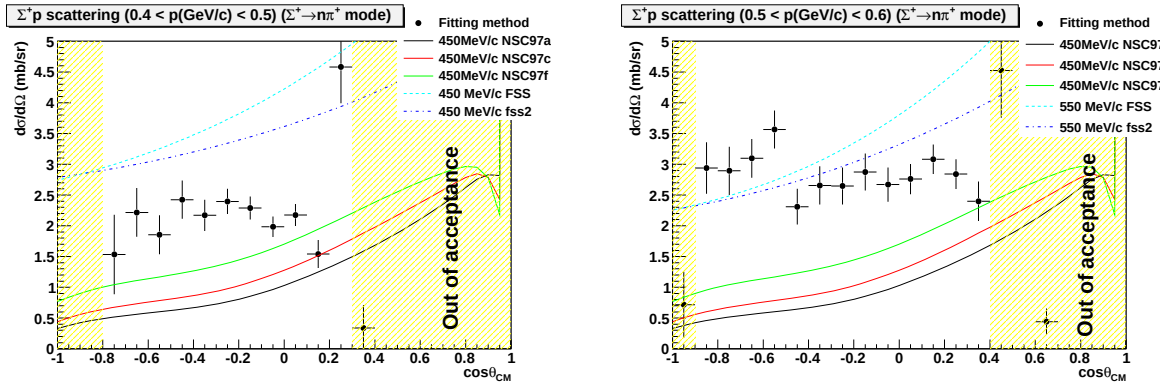

Figure 54: Differential cross section of the $\Sigma^+ p$ elastic scattering in the beam momentum regions of $0.4 < p$ (GeV/c) < 0.5 (left) and of $0.5 < p$ (GeV/c) < 0.6 (left) for the $\Sigma^+ \to n\pi^+$ decay mode. The yellow hatched region shows the region out of acceptance. Theoretical predictions by the OBEP (Nijmegen Soft Core) models and the quark cluster (RGM FSS) models are shown together.

6 Time schedule, cost and man power

We are going to utilize the present detector systems in the K1.8 beam line without much modifications. Additionally, we will construct dedicated detectors to this experiment such as the fiber trackers and the detector system surrounding the LH_2 target. Figure 55 shows the time schedule of the preparation of the newly developed detectors for the proposed experiment. In Table 7, we summarized new items for the proposed experiment.

Since 2009, we have been doing the R&D for the multichannel readout circuit for PPD(MPPC) with a support from KEK and LAL. The SPIROC-A chip is the highly multi-purpose ASIC and we are developing the readout board with SPIROC-A for the fiber trackers. The board has the SiTCP readout which can be incorporated into the present DAQ system. The existing TDC system for the wire chambers can be used for the fiber tracker readout by connecting

the digital output from SPIROC board. We can replace the wire chambers by the beam line fiber tracker in order to handle the high intensity beam.

For the LH_2 target, we will construct a target vessel and vacuum window system with a minimal material so as to detect a low energy proton with a support of a LH_2 target group in KEK.

The detector system around the LH_2 target is the main part of development. We have already made a prototype of the fiber vertex tracker and carried out an test experiment where *pp* scattering is detected at the Cyclotron facility in Tohoku university. The development is on going. For the cylindrical chamber, we will soon start the design works.

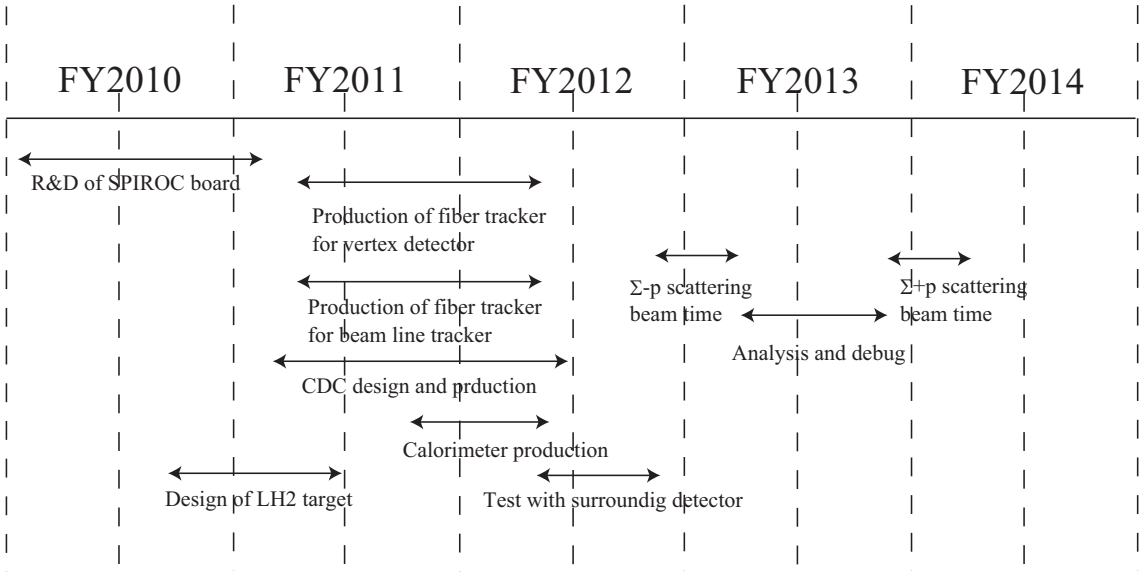

Figure 55: Schedule of the preparation for the proposed experiment

Item		Cost [kJY]
Beam Analyzer		
Fiber tracker	New	1,000
Readout MPPC	New	5,000
SPIROC board	New	10,000
Multihit TDC	Existing	0
LH_2 target	New	5,000
Detector for scattered proton		
Fiber tracker	New	1,000
Readout MPPC	New	4,500
SPIROC board	New	15,000
Cylindrical chamber	New	10,000
Readout Amp & Discri	Reuse of MWPC and MWDC	0
Calorimeter	Reuse of Neutron counter / New	1,000

Table 7: A list of items newly needed for this experiment.

References

[1] M. M. Nagels *et al.*, Phys. Rev. D15 (1977) 2547; D20 (1979) 1633; P. M. Maessen *et al.*, Phys. Rev. C40 (1989) 2226; Th. A. Rijken *et al.*, Nucl. Phys. A547 (1992) 245c.

[2] M. Oka and K. Yasaki, Quarks and Nuclei, et. W. Weise, Vol 1 (World Scientific, 1984) 489; K. Yazaki, Nucl. Phys. A479 (1988) 217c; K. Shimizu, Nucl. Phys. A547 (1992) 265c.

[3] Y. Fujiwara, C. Nakamoto, Y. Suzuki, Prog. Theor. Phys. 94 (1995) 214; 94 (1995) 353; Phys. Rev. Lett. 76 (1996) 2242; Phys. Rev. C54 (1996) 2180.

[4] Y. Fujiwara, Y. Suzuki, C. Nakamoto, Prog. Nucl. Part. Phys. 58 (2007) 439.

[5] T. Inoue *et al.*, HAL QCD collaboration, arXiv:1007:3559 [hep-lat]

[6] R. Engelmann *et al.* Phys. Lett. 21 (1966) 587; B. Sechi-Zorn *et al.* Phys. Rev. 175 (1968) 1735; G. Alexander *et al.* Phys. Rev. 173 (1968) 1452; J. A. Kadyk *et al.* Nucl. Phys. B 27 (1971) 13; F. Eisele *et al.* Phys. Lett. B 37 (1971) 204.

[7] O. Hashimoto and H. Tamura Prog. Nucl. Part. Phys. 57 (2006) 564.

[8] Y. Kondo *et al.* Nucl. Phys. A 676 (2000) 371

[9] J.K. Ahn *et al.* Nucl. Phys. A 761 (2005) 41.

[10] T. Kadowaki *et al.* Eur. Phys. J. A 15 (2002) 295.

[11] J. Asai *et al.* Jpn. J. Appl. Phys. 43 (2004) 1586.

[12] T. Nagae *et al.* Phys. Rev. Lett. 80 (1995) 1605.

[13] H. Noumi *et al.*, Phys. Rev. Lett. 89 (2002) 072301, P.K. Saho *et al.* Phys. Rev. C 70 (2004) 044613.

[14] M. Kohno *et al.* Phys. Rev. C 74 (2006) 064613.

[15] T. Harada and Y. Hirabayashi, Nucl. Phys. A767 (2006) 206.

[16] R. Jastrow, Phys. Rev. 81 (1950) 636.

[17] M.L. Good and R.R. Kofler, Phys. Rev. 183 (1969) 1142.

[18] D.J. Candlin *et al.* Nucl. Phys. B226 (1983) 1.

[19] B. Conforto *et al.* Nucl. Phys. B105 (1976) 189.

[20] http://omega.in2p3.fr/

[21] T. Hamada and I.D. Johnston, Nucl. Phys. 34 (1962) 382.